Mitochondrial fatty acid synthesis coordinates mitochondrial oxidative metabolism

Sara M. Nowinski[1], Ashley Solmonson[7], Scott F. Rusin[8], J. Alan Maschek[2,3,6], Claire L. Bensard[1], Sarah Fogarty[1,5], Mi-Young Jeong[1], Sandra Lettlova[1], Jordan A. Berg[1], Jeffrey T. Morgan[1,5], Yeyun Ouyang[1], Bradley C. Naylor[6], Joao A. Paulo[8], Katsuhiko Funai[2], James E. Cox[1,2,6], Steven P. Gygi[8], Dennis R. Winge[1,2,4], Ralph J. Deberardinis[5,7], and Jared Rutter[1,2,5]

[1]Department of Biochemistry; [2]Diabetes & Metabolism Research Center; [3]Department of Nutrition and Integrative Physiology, [4]Department of Internal Medicine, [5]Howard Hughes Medical Institute, and [6]Metabolomics, Proteomics and Mass Spectrometry Core Research Facilities University of Utah, 15 N. Medical Dr. East, Salt Lake City, UT, 84112, USA.

[7]Children's Medical Center Research Institute, University of Texas Southwestern Medical Center, 5323 Harry Hines Boulevard, Dallas, TX 75390, USA.

[8]Department of Cell Biology, Harvard University School of Medicine, Boston, MA 02115, USA.

Correspondence:

rutter@biochem.utah.edu (J.R.)

Abstract:

Cells harbor two systems for fatty acid synthesis, one in the cytoplasm (catalyzed by fatty acid synthase, FASN) and one in the mitochondria (mtFAS). In contrast to FASN, mtFAS is poorly characterized, especially in higher eukaryotes, with the major product(s), metabolic roles, and cellular function(s) being essentially unknown. Here we show that hypomorphic mtFAS mutants display a severe loss of electron transport chain (ETC) complexes and exhibit compensatory metabolic activities including reductive carboxylation. This effect on ETC complexes appears to be independent of protein lipoylation, the best characterized function of

mtFAS, as mutants lacking lipoylation have an intact ETC. Finally, mtFAS impairment blocks the differentiation of skeletal myoblasts *in vitro*. Together, these data suggest that ETC activity in mammals is profoundly controlled by mtFAS function, thereby connecting anabolic fatty acid synthesis with the oxidation of carbon fuels.

Keywords:
Mitochondria, fatty acid synthesis, electron transport chain, reductive carboxylation, lipoylation, TCA cycle, metabolism, respiration, OXPHOS, muscle

Abbreviations:
ACP – acyl carrier protein, ETC – electron transport chain, FAS – fatty acid synthesis, FASN – fatty acid synthase, LYRM – leucine tyrosine arginine motif, mtFAS – mitochondrial fatty acid synthesis, OGDH – oxoglutarate dehydrogenase, OXPHOS – oxidative phosphorylation, PAGE – polyacrylamide gel electrophoresis, PDH – pyruvate dehydrogenase, TCA – tricarboxylic acid

42 **Introduction**

43

44 Fatty acids play diverse cellular roles, including providing the hydrophobic tails of membrane
45 phospholipids, energy storage in the form of triglycerides, and as cell signaling molecules. Aside
46 from the import of exogenous fatty acids, mammalian cells use the well-known and well-studied
47 cytoplasmic enzyme fatty acid synthase (FASN) to make palmitate, which is further modified to
48 form the diverse array of cellular fatty acids (Smith, 1994). However, it is much less appreciated
49 that mitochondria also harbor a spatially and genetically distinct fatty acid synthesis pathway
50 (mtFAS) (reviewed in (Nowinski et al., 2018)). In contrast to FASN, which is a very large protein
51 that contains several domains and encompasses all of the enzymatic activities necessary for
52 FAS condensed in a single polypeptide chain, the mtFAS pathway is comprised of at least six
53 enzymes all encoded by separate genes. These enzymes catalyze sequential steps to achieve
54 one cycle of two-carbon addition to a growing acyl chain (Figure 1A). The nascent fatty acids
55 are covalently attached to the mitochondrial acyl carrier protein (ACP), which acts as a soluble
56 scaffold upon which the acyl chains are built. In each cycle of the pathway, malonyl-CoA is
57 converted to malonyl-ACP, which then undergoes a condensation reaction with the growing fatty
58 acyl chain on ACP, extending the chain by two carbons and releasing a CO_2 molecule.
59 Thereafter, the remaining enzymes in the pathway must carry out a series of reduction and
60 dehydration reactions to fully reduce the acyl chain to a saturated fatty acid, which is the
61 substrate for further cycles of two-carbon addition. Among the several differences between
62 MtFAS and cytoplasmic FAS, FASN exclusively produces palmitate, whereas mtFAS appears to
63 have at least two major products.

64 Although the human genes responsible for each step in the mtFAS pathway have been
65 identified, and their ability to complement the orthologous mutants in yeast has been
66 demonstrated (Autio et al., 2008; Chen et al., 2009; Joshi et al., 2003; Miinalainen et al., 2003;
67 Zhang et al., 2005; Zhang et al., 2003), few loss-of-function studies have examined the

68 consequences of mtFAS deficiency in mammalian systems. Inducible knockout of the
69 mitochondrial malonyl CoA-acyl carrier protein transacylase (*Mcat*) using a Cre driver that
70 expresses in most tissues in mice results in a severe phenotype characterized by weight loss,
71 reduced muscle strength, and shortened lifespan despite the persistence of residual MCAT
72 protein (Smith et al., 2012). Knockout of the mitochondrial 2-enoyl thioester reductase, *Mecr*, is
73 lethal in mice due to a placental defect (Nair et al., 2017), while the inducible knockout of *Mecr*
74 specifically in Purkinje cells leads to loss of this cell population and recapitulates many
75 phenotypes of MePaN syndrome, the human disease caused by *Mecr* mutation (Gorukmez et
76 al., 2019; Heimer et al., 2016; Nair et al., 2018). Similarly, *Mecr* knockdown has been shown to
77 inhibit the growth of hepatocellular carcinoma cells (Cai et al., 2019). While these detrimental
78 phenotypes are clear, the molecular consequences of mtFAS loss remain poorly understood.
79 MtFAS currently has one known product: an eight-carbon saturated fatty acid, octanoate,
80 that is subsequently converted to lipoic acid. This important cofactor is required for the catalytic
81 activity of a number of mitochondrial enzymes, most notably pyruvate dehydrogenase and α-
82 ketoglutarate dehydrogenase (Brody et al., 1997; Wada et al., 1997), but also branched chain
83 amino acid dehydrogenase, the H protein of the glycine cleavage system, and 2-oxoadipate
84 dehydrogenase (reviewed in (Solmonson and DeBerardinis, 2018)). This observation, made
85 more than 20 years ago, has guided mtFAS-focused research for the past two decades. Studies
86 have shown that loss of lipoic acid synthesis and/or failure to efficiently transfer lipoic acid to its
87 target proteins is lethal in mice (Ni et al., 2019; Yi and Maeda, 2005), and attributed other
88 mitochondrial changes as downstream of lipoic acid synthesis (Smith et al., 2012). However,
89 though the mouse studies described above have demonstrated striking phenotypes that result
90 from loss of mtFAS, they fail to distinguish between direct effects of loss of protein lipoylation
91 versus loss of other mtFAS function(s). Although lipoic acid unmistakably has important central
92 functions in mitochondrial metabolism, there is reason to be skeptical that the sole function of
93 mtFAS is the production of lipoic acid.

In addition to the eight-carbon precursor for lipoic acid, it is clear that mtFAS also produces longer acyl chains of at least 14 carbons, yet the identity of these lipids and their cellular functions are uncertain (Angerer et al., 2017; Witkowski et al., 2007). Perhaps more surprisingly, these longer acyl chains appear to partially be maintained in attachment to ACP (Angerer et al., 2017), further complicating the question of their cellular functions. We set out to systematically examine the cellular functions of the mtFAS pathway by mutating genes that encode three distinct steps in the pathway, *Mcat*, *Oxsm*, and *Mecr*. For comparison, we also engineered cells with loss of *Lipt1*, the terminal enzyme in the production of lipoylated enzymes downstream of mtFAS. We found that several phenotypes resulting from loss of the mtFAS pathway are not related to lipoic acid, but must instead be due to loss of other products or functions of mtFAS. In particular, we find that loss of mtFAS, but not lipoic acid synthesis, leads to a profound impairment in the assembly of the mitochondrial electron transport chain machinery, with the attendant consequences on metabolism and cell behaviors. Our data therefore suggest that the mtFAS pathway acts as a key regulator of mitochondrial respiratory metabolism.

Results

Mitochondrial fatty acid synthesis is an essential pathway that does not contribute to synthesis of cellular lipids

The enzymes of mtFAS are ubiquitously expressed in mammalian tissues, with the highest expression in skeletal muscle and heart (Triepels et al., 1999). Therefore, we chose cultured skeletal myoblasts as a model system in which to examine the role of this pathway. We employed a CRISPR/Cas9-based strategy to mutate three genes encoding enzymes in the mtFAS pathway, using two different guide RNA sequences per gene. We targeted *Mcat*, encoding the malonyl-CoA ACP transacylase, *Oxsm*, encoding the beta-ketoacyl synthase that

120 condenses malonyl-ACP with the growing acyl chain, and *Mecr*, encoding the terminal
121 reductase in each cycle of two-carbon unit addition (Figure 1A). It is important to note that
122 because mtFAS is a cycle that requires all enzymes for each stepwise two-carbon addition, loss
123 of each individual enzyme blocks fatty acid synthesis at an early, albeit distinct step. *Mcat*
124 mutants should be unable to attach any carbon to ACP, whereas *Oxsm* mutants should be able
125 to produce malonyl-ACP, and *Mecr* mutants could at most build short four-carbon acyl chains.
126 We observed roughly 70-80% editing efficiency for all six of the guides utilized (based on T7E1
127 assays, data not shown). We found that transfection with Cas9 and sgRNAs targeting mtFAS
128 genes led to smaller colonies at one-week post-single cell sorting relative to control guides
129 (Figure supplement 1A). Many of the smallest clones stopped growing and/or did not survive
130 expansion. After screening more than 100 of the surviving single cell clones, we failed to identify
131 a single null mutant for any of the three genes targeted. This finding was not altogether
132 unexpected, given that at least one other knockdown study concluded that NDUFAB1, the
133 mammalian mitochondrial ACP, is essential in HEK293T cells (Feng et al., 2009). Indeed, The
134 Broad Institute's Depmap lists NDUFAB1 as a "common essential" gene, and the mtFAS genes
135 all display negative gene effects, indicating they are essential in at least some cell lines (Broad,
136 2020). Taken together, our results strongly support the conclusion that the mtFAS pathway is
137 essential in cultured skeletal myoblasts.
138 Although no complete null clones were generated, we were able to isolate several clonal cell
139 lines with markedly decreased abundance of MCAT, OXSM, and MECR. These clones also had
140 no detectable lipoylation of PDH and OGDH subunits (DLAT and DLST, respectively) in isolated
141 mitochondrial fractions (Figure 1B), and grew slowly relative to control clones (Figure
142 supplement 1B). MECR has been reported to have dual localization to the cytoplasm in addition
143 to mitochondria (Kim et al., 2014), so we performed sub-cellular fractionation to assess these
144 two MECR populations in our mutant cells. We observed an overall decrease in MECR
145 expression that was most pronounced in the mitochondrial compartment (Figure supplement

146 1C). We thus moved forward with the characterization of these presumably hypomorphic cell
147 lines.

148 As mentioned previously, the canonical function of mtFAS is the production of octanoate,
149 the eight-carbon precursor for lipoic acid synthesis. However, some have speculated that
150 mtFAS might also generate fatty acids that contribute to phospholipid synthesis. Seminal
151 studies found 3-hydroxymyristate as the predominant acyl modification on mitochondrial ACP in
152 fungi (Mikolajczyk and Brody, 1990; Schneider et al., 1997). A more recent effort to identify the
153 predominant lipid species found a variety of medium and long chain acyl species, raising the
154 possibility of multiple products in addition to octanoate (Angerer et al., 2017). Although mtFAS
155 mutant yeast display changes in steady-state lipids, the interpretation of this observation is
156 confounded by other phenotypes of these cells (Schneider et al., 1995). In the only study that
157 examines the role of mtFAS in lipid synthesis in mammals, transient knockdown of ACP did not
158 change the abundance of mitochondrial lipids; however, this does not exclude the possibility
159 that cytoplasmic FAS can compensate for loss of mtFAS (Clay et al., 2016).

160 We therefore set out to test whether mtFAS contributes to cellular phospholipid pools in the
161 presence and absence of the cytosolic fatty acid synthase, FASN. In wild type and *Oxsm* mutant
162 cell lines, we stably expressed hairpins targeting *FASN*, which encodes the cytoplasmic fatty
163 acid synthase, or a scrambled control (Figure 1C). We then fed the cells uniformly labeled ^{13}C-
164 glucose and observed labeling in cellular lipids to define the relative contributions of cytoplasmic
165 FAS and mtFAS to various cellular lipid pools. By monitoring accumulation of the m+2
166 isotopologue over time, we observed a dependence on FASN expression, but not mtFAS for the
167 synthesis of new phospholipids (shown are two representative PC species, Figure 1D & 1E).
168 Higher order isotopologues from additional cycles of elongation by fatty acid synthesis (e.g. m +
169 4, m + 6, m + 8, and so on) did not show labeling above background in this experiment.
170 Similarly, fatty acid methyl esther analysis (FAMES) showed an effect of *FASN* knockdown, but
171 not *Oxsm* mutation, on incorporation of U^{13}C-glucose into c16:0 and c18:0 lipids, which

172 confirmed that the m+2 labeling of phospholipids is likely in the fatty acid tails (Figure
173 supplement 1D). These experiments demonstrate that longer acyl chains synthesized by mtFAS
174 do not contribute to cellular fatty acid and phospholipid pools and likely perform some other
175 function.
176
177 **Mutation of mtFAS results in a profound mitochondrial respiratory phenotype and loss of**
178 **ETC complexes**
179
180 Given the known and hypothesized functions of mtFAS, we next assayed mitochondrial
181 function in the mtFAS mutant cells. We performed a standard Seahorse mitochondrial stress
182 test in high glucose media and found that the mtFAS mutant cells displayed a roughly 30-40%
183 decrease in basal respiration rate compared with controls (Figure 2A). More strikingly, the
184 mtFAS mutants exhibited a lack of spare respiratory capacity, with FCCP-stimulated uncoupled
185 respiration rates that were similar to the initially measured basal respiration (Figure 2A).
186 Interestingly, *Oxsm* and *Mecr* mutants exhibited an increased basal extracellular acidification
187 rate, suggesting that these cell lines compensate for decreased respiration via increased
188 glycolysis, whereas *Mcat* mutants do not (Figure supplement 2A). In agreement with the
189 observed decrease in cellular respiration, mtFAS mutants also show a markedly decreased
190 mitochondrial membrane potential, as measured by the ratio of MitoTracker Red to MitoTracker
191 Green fluorescence (Figure 2B,C and Figure supplement 2B).
192 Concurrent decreases in mitochondrial membrane potential and respiration can have
193 several causes ranging from altered substrate utilization and TCA cycle activity to decreased
194 expression and/or activity of electron transport chain (ETC) complexes. Therefore, we examined
195 OXPHOS complex expression and assembly via blue-native PAGE analysis. Strikingly, fully
196 assembled ETC complex I (CI), complex II (CII), and complex IV (CIV) were almost completely
197 absent in mtFAS mutant mitochondria (Figure 2D). Complex V was also decreased in

198 abundance, albeit to a lesser magnitude than that seen for CI, CII, and CIV. In contrast,
199 complex III (CIII) was relatively unaffected by loss of mtFAS, although CIII-containing
200 supercomplexes (SC) were absent, likely resulting from loss of CI and CIV. Furthermore, while
201 CIII abundance and assembly were relatively unaffected, its activity was reduced in each of the
202 mtFAS-deficient cells (Figure supplement 2C). Altogether, these results depict a severe
203 respiratory deficiency in mtFAS mutant cells, characterized by the striking loss of stably
204 assembled OXPHOS complexes in mtFAS mutant mitochondria. Notably, this contrasts sharply
205 with FASN, deletion of which does not affect fatty acid oxidation in muscle (Funai et al., 2013).
206
207 **mtFAS supports ETC assembly via the post-translational stabilization of LYRM proteins**
208
209 To further examine the mechanisms underlying loss of ETC complexes in mtFAS mutant
210 cells, we performed an unbiased quantitative proteomics experiment on duplicate whole cell
211 lysates from three mtFAS mutant clones (one *Oxsm* and two *Mecr* mutants) and two control
212 clones. Overall, there was no general trend for the steady-state abundance of mitochondrial
213 proteins, with 77 proteins being statistically more abundant and 34 proteins being decreased in
214 abundance (Figure 3A). We also observed that the majority of the proteins that comprise
215 OXPHOS complexes were likewise similar in abundance between control and mtFAS mutant
216 cells, including those in Complexes I, II and IV (Figure 3A,B), despite the decrease in
217 abundance of the completely assembled complexes by blue-native PAGE (Figure 2D).
218 However, a subset of eight OXPHOS proteins displayed significantly decreased abundance in
219 both *Oxsm* and *Mecr* mutant cell lines compared to controls, including NDUFA6, NDUFA12,
220 NDUFS4, NDUFS6, SDHB, COX5a, COX5b, and ATPIF1 (Figure 3A,B). To test whether these
221 changes were transcriptional, we performed RNAseq analysis on control and mtFAS mutant
222 cells. However, we found no significant changes in the abundance of transcripts encoding ETC

223 component proteins (Figure 3C and Figure supplement 3A-C), implying that the observed
224 decrease in abundance of these proteins is likely due to post-translational regulation.
225 The two proteins that were most decreased in abundance, NDUFA6 and SDHB (Figure
226 3D,E), also stood out because of their relationships with the leucine-tyrosine-arginine motif
227 (LYRM) protein family, a family of small proteins chiefly comprised of late-stage ETC assembly
228 factors (Angerer, 2015). In many cases, such as for Complex II, LYRM proteins (SDHAF1 and
229 SDHAF3) bind to and facilitate the insertion of a target protein (in this case SDHB) in the final
230 stage of ETC complex assembly (Ghezzi et al., 2009; Na et al., 2014). In other cases, such as
231 for Complex I, the LYRM proteins NDUFA6 and NDUFB9 are actually stable subunits of the fully
232 assembled complex (Fiedorczuk et al., 2016; Zhu et al., 2016). LYRM proteins are also found as
233 a stable component of the NFS-containing iron-sulfur cluster biogenesis (ISC) complex
234 (LYRM4) as well as in an assembly intermediate of the mitochondrial ribosome (AltMid51)
235 (Boniecki et al., 2017; Brown et al., 2017). High-throughput interactomics studies in mammalian
236 systems and targeted experiments in yeast have identified physical interactions between ACP
237 and several LYRM proteins (Floyd et al., 2016; Huttlin et al., 2015; Majmudar et al., 2019; Van
238 Vranken et al., 2018). Interestingly, the ACP protein found in complex with LYRM proteins
239 appears often to have maintained its acyl modification, which is generated through the
240 sequential actions of the mtFAS enzymes as described above (Angerer et al., 2014; Cory et al.,
241 2017; Runswick et al., 1991; Van Vranken et al., 2016). Studies have shown that the acyl chain
242 on ACP is intimately involved in these physical interactions, folding into the middle of the LYRM
243 proteins, but the role of ACP acylation in its varied functions is mostly untested (Angerer et al.,
244 2017; Boniecki et al., 2017; Cory et al., 2017; Fiedorczuk et al., 2016; Zhu et al., 2016).
245 In addition to the structurally verified ACP-LYRM interactions, three other LYRM family
246 members with known target proteins have been suggested to interact with ACP based on high-
247 throughput interactomics studies: SDHAF1 and SDHAF3, discussed above, and LYRM7, which
248 mediates the addition of UQCRFS1 in the last step of complex III assembly (Floyd et al., 2016;

249 Huttlin et al., 2015; Na et al., 2014; Sanchez et al., 2013). Thus, we hypothesized that the
250 decreased abundance of SDHB (Figure 3E) could be explained by interaction of ACP with
251 SDHAF1 and/or SDHAF3. To verify whether ACP in fact interacts with these additional LYRM
252 family members, we expressed epitope-tagged variants of ACP and each LYRM in cells and
253 confirmed their physical interaction via co-immunoprecipitation and immunoblotting (Figure
254 supplement 3D). Along with other published data (Van Vranken et al., 2018), the finding that
255 NDUFA6, a known LYRM protein, and SDHB, the target of two known LYRM proteins, exhibit
256 decreased abundance in mtFAS mutant cell lines supports the hypothesis that interaction with
257 an acylated ACP is required for the complex assembly functions of these LYRM proteins.
258 This finding prompted us to examine the abundance of other LYRM proteins and their
259 targets in the mtFAS mutant cell lines. Indeed, LYRM4 and its target NFS1 were also
260 significantly decreased in abundance in our whole cell proteomics dataset, implying that LYRM4
261 also requires acylated ACP for the stability and function of itself and NFS1 (Figure 3F,G).
262 Interestingly, NDUFB9, the other CI LYRM, and UQCRFS1, a subunit of CIII and the target of
263 LYRM7, were not significantly decreased in abundance in mtFAS mutant cells (Figure
264 supplement 3E,F), implying that either the interactions between ACP and these LYRM proteins
265 is not dependent on acylation and mtFAS, or that other compensatory mechanisms are at play.
266 We performed immunoblot analysis of UQCRFS1 and found that it was also decreased in
267 abundance similarly to other LYR targets, perhaps explaining the observed decrease in CIII
268 activity despite the partial maintenance of complex assembly (Figure 3H).
269 Finally, ACP has also been found to interact with an assembly intermediate of the
270 mitochondrial ribosome through a novel LYRM protein called altMiD51 and its target, MALSU1
271 (Brown et al., 2017). Brown et al. proposed that this interaction might negatively regulate
272 mitochondrial translation because MALSU1, altMiD51, and ACP bind the large mitochondrial
273 ribosomal subunit in a way that precludes small subunit binding, but the role of ACP acylation in
274 this interaction is unclear (Brown et al., 2017; Dibley et al., 2020; Rathore et al., 2018). Despite

275 this proposed role of ACP in mitochondrial translation, we found that the abundance of
276 mitochondrially encoded proteins was unchanged in the mtFAS mutant cell lines (Figure
277 supplement 3G). Importantly, this includes MTCO1 and MTCO2, two subunits of CIV, strongly
278 implying that the diminution of CIV in mutant cells does not result from loss of mitochondrial
279 translation. Interestingly, however, MALSU1 was significantly decreased in abundance (Figure
280 supplement 3H), which raises the possibility that MALSU1 downregulation might be a
281 compensatory adaptation that the cells make to avoid collapse of mitochondrial translation upon
282 loss of mtFAS.
283
284 **Impairment of mtFAS induces reductive labeling of TCA cycle intermediates**
285
286 The profound defects observed in mitochondrial respiration led us to examine mitochondrial
287 and cellular metabolism more comprehensively in our mtFAS mutants. We first performed
288 steady-state metabolomics analysis on control and mtFAS mutant cells. Purines were among
289 the most significantly depleted metabolites in mtFAS mutants, but we observed no change in
290 pyrimidines (Figure supplement 4A,B, all measured metabolites in Supplementary Table 1).
291 Purine depletion may be a result of decreased activity of another lipoylated protein – the glycine
292 cleavage H protein, which plays a role in purine biosynthesis (Fujiwara et al., 1991). mtFAS
293 mutants exhibited robust pyruvate accumulation, in agreement with the decreased lipoylation
294 and reduced activity of PDH, but only a minor and statistically insignificant increase in
295 intracellular lactate (Figure 4A and Figure supplement 4C). Similarly, no significant changes
296 were observed in the abundance of glutamine or glutamate (Figure supplement 4D,E). In
297 contrast, the TCA cycle intermediates citrate, fumarate, and malate all showed significantly
298 decreased abundance (Figure 4B-D). Aspartate, the synthesis of which requires the TCA cycle
299 metabolite oxaloacetate and an electron acceptor such as the ETC (Birsoy et al., 2015; Sullivan
300 et al., 2015), was strongly depleted in the mtFAS mutant cells (Figure 4E).

301 To further understand how TCA cycle metabolism is affected by impairment of mtFAS, we
302 fed the cells uniformly labelled ^{13}C-glutamine for 24 hours and assessed labeling of TCA cycle
303 intermediates to monitor glutamine contribution to TCA cycle flux (schematic in Figure 4F). This
304 experiment led to three observations that were particularly interesting. First, glutamate cycling in
305 the TCA cycle is decreased in the mtFAS mutant cells. We observed no differences in glutamine
306 uptake in mutant cells compared to controls (Figure supplement 4F). However, in pre-steady
307 state measurements we observed reduced labeling of glutamate in mtFAS mutants (Figure
308 supplement 4G). Furthermore, after 24 hours of labeling, the mtFAS-deficient cells showed
309 reduced fractional enrichments of the glutamate m+3 and m+1 isotopologues, which are
310 synthesized on subsequent turns of the TCA cycle (Figure 4G). In contrast, the m+5
311 isotopologue contributes a larger fraction of the total pool (Figure 4G). These data are
312 consistent with decreased processivity of the TCA cycle in cells lacking mtFAS.
313 Secondly, we observed that labeling of TCA cycle intermediates shows a clear distinction
314 between succinate and later metabolites. Like glutamate, succinate labeling is initially slow
315 (Figure supplement 4H). After 24 hours in ^{13}C-glutamine, however, similar to what we observe
316 for glutamate labeling, in control cells subsequent rounds of the TCA cycle cause m+2
317 succinate to accumulate. In mtFAS mutant cells, m+2 succinate labeling is reduced while m+4
318 accumulates, indicating its decreased cycling in the TCA cycle (Figure 4H). In contrast, m+4
319 labeling of fumarate, malate, and citrate are all markedly lower at short time points (Figure
320 supplement 4I-K), and remain low after 24 hours (Figures 4I-K), along with m+4 aspartate,
321 which is derived from m+4 citrate (Figure 4L). These data and the reduced abundances of
322 fumarate and malate support a block of the TCA cycle at the succinate dehydrogenase (SDH)
323 catalyzed step, and is in agreement with our data that demonstrate decreased steady state
324 SDHB stability and a near-complete loss of fully assembled Complex II (Figures 2D and 3H).
325 Finally, the third observation we made from these data is that mtFAS mutants displayed
326 significantly increased levels of m+5 citrate (Figure 4K), which is formed from the reductive

327 carboxylation of α-ketoglutarate, and is the canonical marker of reductive carboxylation.
328 Accordingly, we also saw significant increases in m+3 fumarate, malate, and aspartate (Figures
329 4I,J and L), which are formed from this pathway downstream of m+5 citrate (Mullen et al.,
330 2012). Previous analysis of the reductive pathway concluded, as we observed here, that cells
331 with ETC defects continue to produce succinate by the oxidative pathway, perhaps to generate
332 reducing equivalents to drive reductive carboxylation(Mullen et al., 2014). In summary, these
333 data support the conclusion that oxidative cycling of TCA cycle intermediates is decreased
334 overall, with a particular block at the SDH-catalyzed step. Furthermore, mtFAS mutants invoke
335 reductive carboxylation to produce citrate, and reductive labeling of downstream metabolites is
336 also increased. Reductive carboxylation is often seen in models of ETC inhibition or mutation
337 (Mullen et al., 2011) and further supports the model that mtFAS mutants display significant ETC
338 dysfunction.
339
340 **Loss of ETC assembly and reductive carboxylation are not downstream of loss of protein**
341 **lipoylation.**
342
343 The best-studied function of mtFAS is the biosynthesis of octanoate, the eight-carbon
344 precursor of lipoic acid, but it also produces longer acyl chains. This raises the possibility that
345 there are at least two independent mechanisms whereby mtFAS might act on mitochondrial
346 function: one via lipoic acid synthesis and another in which these longer acyl chains facilitate the
347 acyl-ACP dependent activation of LYRM proteins in ETC complex assembly. Therefore, we
348 decided to determine whether the metabolic phenotypes observed in mtFAS mutant cells are
349 also found in cells containing an intact mtFAS system, but lacking the ability to transfer lipoic
350 acid to target proteins, including the 2-ketoacid dehydrogenases (2KADHs). We created mutant
351 cell lines for *Lipt1*, the gene that encodes the terminal enzyme in protein lipoylation (Figure 5A).
352 In these mutants, synthesis of octanoate and longer acyl chains by mtFAS should be

353 unaffected, as Lipt1 catalyzes the terminal step in lipoic acid transfer to its target proteins
354 downstream of mtFAS (reviewed in (Solmonson and DeBerardinis, 2018)). Similar to mtFAS
355 mutants, *Lipt1* mutant cells displayed undetectable protein lipoylation (Figure 5A). The fact that
356 mtFAS mutants and *Lipt1* mutants both have drastically reduced protein lipoylation, below the
357 limit of detection via western blotting, allows us to attribute any phenotypes observed in mtFAS
358 mutants that are not phenocopied by *Lipt1* mutants to non-lipoic acid products of mtFAS.
359 Like mtFAS mutants, Lipt1 mutants display an analogous, albeit somewhat milder
360 respiratory phenotype (Figure 5B). However, in sharp contrast to the destabilization of ETC
361 complexes observed in mtFAS mutants, *Lipt1* mutants largely maintain an assembled ETC, with
362 similar levels of CI, CII, and SC as in control cells (Figure 5C). Notably, CV was more
363 destabilized in *Lipt1* mutants than in mtFAS mutants, suggesting a mtFAS-independent mode of
364 CV regulation by LIPT1 outside of lipoic acid (Figure 5C). Nevertheless, it appears that the
365 mtFAS-dependent regulation of CI and CII is essentially independent of lipoic acid synthesis
366 and therefore likely involves some other lipid product of mtFAS.
367 Finally, we wanted to determine which portions of the metabolic phenotypes resulting from
368 mtFAS loss are attributable to loss of protein lipoylation. We found that, in contrast to mtFAS
369 mutants, *Lipt1* mutants had normal abundance of TCA cycle metabolites (Figure 5D). $U^{13}C$-
370 glutamine flux experiments showed that LIPT1 loss caused a reduction in oxidative labeling and
371 at most a small increase in reductive labeling of fumarate and malate (Figure 4E), consistent
372 with its small effects on OCR and ETC assembly and with similar labeling effects in fibroblasts
373 from LIPT1-deficient patients (Ni et al., 2019). In all, our data strongly support a model in which
374 mtFAS-dependent acyl chains facilitate acyl-ACP/LYRM interactions to support the biosynthesis
375 of ETC complexes independent of lipoic acid.
376
377 **Impairment of mtFAS impedes skeletal myoblast differentiation**
378

379 C2C12 myoblasts are muscle precursor cells that remain proliferative in culture unless
380 stimulated to terminally differentiate. However, upon examination of the quantitative proteomics
381 experiment described above, we noticed that the largest group of proteins with decreased
382 abundance were all related to the terminal differentiation of muscle cells (Figure 6A,
383 Supplementary Table 2). Although some of these differences did not reach statistical
384 significance, likely due to the low abundance of these proteins in proliferative myoblast cultures,
385 we were nonetheless intrigued by this observation, which might imply a defect in myoblast
386 differentiation. Indeed, when treated with differentiation medium for up to seven days, mtFAS
387 mutant cell lines almost completely failed to differentiate, as monitored by the formation of
388 multinucleated myotubes (Figure 6B and Figure supplement 6A).
389 Muscle cell differentiation is controlled by a transcription factor cascade in which MyoD
390 activates the transcription of Myogenin (Myog), and Myog in turn activates the transcription of
391 many terminal differentiation genes, such as myosin heavy chain (MHC, encoded by *Myh1*)
392 (Zammit, 2017). To further explore the effect of mtFAS mutation on differentiation, we
393 immunoblotted for MyoD, Myog, and MHC in proliferative conditions (day −1) and at 1, 3, and 7
394 days of culture in differentiation medium. Although MyoD expression was largely unaffected in
395 mtFAS mutant cells, Myog induction appeared to be decreased or absent in mtFAS cells (Figure
396 6C). Similarly, the Myog target protein MHC was almost undetectable in mtFAS mutant cells
397 (Figure 6C). To further explore the mechanism underlying impairment of Myog induction and
398 muscle cell differentiation, we performed RNA-Seq analyses on cells grown at early time points
399 in differentiation (day −1, day 0, and day 1). The results confirmed no difference in *MyoD*
400 transcript expression, but showed both a delay and blunting of induction of the *Myog* transcript
401 as well as those of its target genes such as *Myh1* and myogenic differentiation genes generally
402 (Figure 6D,E and Figure supplement 5B-D). Another Myog target, the transcription factor Mef2c,
403 is also involved in the feed forward propagation of the myogenic program (Ji et al., 2009;
404 Rogerson et al., 2002). Interestingly, in two of the three mtFAS mutant clones assayed, *Mef2c*

405 transcripts were also strikingly down-regulated compared with control (Figure 6D,E), which
406 raises the possibility that it plays a particularly important role in the connection of mtFAS and
407 mitochondrial metabolism with myocyte differentiation.
408 *Myog* induction and myogenic differentiation requires extensive epigenetic remodeling (Asp
409 et al., 2011). Several cellular demethylases, including DNA demethylases and Jumonji histone
410 demethylases use alpha-ketoglutarate (αKG) as a methyl acceptor, and the αKG to succinate
411 ratio has been shown to affect demethylase activity (Pavlova and Thompson, 2016; Soloveychik
412 et al., 2016). Steady state metabolomics analysis of mtFAS mutant cell lines revealed a large
413 increase in αKG as well as in the αKG/succinate ratio (Figure 6F), suggesting a possible
414 mechanism for the impairment of *Myog* induction and myocyte differentiation.
415
416 **Discussion**
417
418 Here we have shown that three genes in the mtFAS pathway (*Mcat*, *Oxsm*, and *Mecr*) are
419 likely essential in cultured mammalian skeletal myoblasts. Hypomorphic mutants of these genes
420 lead to loss of detectable protein lipoylation, without affecting structural phospholipids such as
421 PC. Strikingly, mtFAS impairment results in a profound mitochondrial phenotype characterized
422 by loss of assembled ETC complexes I, II, and IV. Quantitative proteomics analysis revealed the
423 specific decreases in the abundance of two LYRM proteins, NDUFA6, a subunit of CI, and
424 LYRM4, a member of the ISC complex, along with its target protein, NFS1, and another LYRM
425 target, SDHB. Importantly, the LYRM proteins that coordinate SDHB in CII assembly, SDHAF1
426 and SDHAF3, were not identified in our proteomics dataset, however we infer that they are likely
427 also decreased in abundance in mtFAS mutant cells, giving rise to the observed effect on
428 SDHB. RNA-Seq analyses confirmed that the decreased abundance of these proteins is not a
429 result of transcriptional down-regulation, but likely reflects post-translational destabilization. Our

430 data together with that from multiple other eukaryotic model systems support a model in which
431 this effect is mediated through the physical interaction of acyl-ACP with LYRM proteins,
432 resulting in their acylation-dependent activation and functional assembly of ETC complexes
433 (Angerer et al., 2017; Van Vranken et al., 2018).

434 Like mtFAS mutants, *Lipt1* mutants lose any detectable protein lipoylation and have
435 impaired mitochondrial respiration. However, the acylation-dependent activation of LYRM
436 proteins and ETC complex assembly appears to require lipid products of mtFAS other than
437 lipoic acid, as although *Lipt1* mutants lose protein lipoylation, they maintain mitochondrial ETC
438 complexes I-IV. This finding is supported by studies in yeast that reached a similar conclusion
439 based upon a suppressor mutation which can rescue OXPHOS in the absence of lipoic acid
440 restoration (Kursu et al., 2013; Van Vranken et al., 2018). We also found that mtFAS mutants
441 and *Lipt1* mutants both undergo significantly decreased oxidative TCA cycling, however only
442 mtFAS mutants appear to display decreased abundance of TCA cycle intermediates and
443 robustly employ reductive carboxylation. We infer that these metabolic effects are likely
444 downstream of loss of ETC complex function, as has been previously reported in the literature
445 (Mullen et al., 2011). As both mtFAS mutants and *Lipt1* mutants have undetectable lipoic acid
446 levels, but only mtFAS mutants have impaired synthesis of longer acyl chains on ACP, these
447 data suggest that it is these longer acyl chains that are important for the interaction of acyl-ACP
448 and activation of LYRM proteins. These findings also have implications for how patients with
449 mutations in the lipoic acid pathway vs. the mtFAS pathway are treated.

450 It is important to note that some of the effects we observe on ETC assembly cannot be
451 explained by the known interactions between LYRMs and acyl-ACP. For example, it is unclear
452 how mtFAS impairment leads to the instability of Complex IV. One possibility is simply that CIV
453 is less stable outside of its association with respiratory supercomplexes, which are almost
454 completely absent in mtFAS mutant cells, likely as a result of Complex I loss. Alternatively,
455 COX5A and COX5B are among the most affected ETC subunits by proteomics, and could be

456 the targets of either a novel LYRM protein or another mtFAS-dependent mechanism. In
457 mammals, the LYRM family includes at least eleven proteins but as this motif is degenerate and
458 poorly defined, there are likely to be many that are still undiscovered. Of the currently annotated
459 LYRM proteins, at least three (LYRM1, LYRM2, and LYRM9) have no known molecular target,
460 although LYRM2 has recently been implicated in CI assembly in addition to NDUFA6 and
461 NDUFB9 (Dibley et al., 2020). The extent to which these novel LYRM proteins require ACP
462 acylation for function is also unknown.

463 Similarly, further study into the difference(s) between LYRMs that depend on ACP acylation
464 and those that do not is warranted. As mentioned above, we observed decreases in abundance
465 of two LYRM proteins, NDUFA9 and LYRM4, and can infer the destabilization of SDHAF1 and
466 SDHAF3 from the decreased abundance of SDHB. Conversely, we did not observe
467 destabilization of NDUFB9 and UQCRFS1 upon mtFAS mutation, implying that NDUFB9 and
468 LYRM7 are not dependent on ACP acylation for their stability and functions, although orthologs
469 in other eukaryotes seemed to be (Angerer et al., 2017; Van Vranken et al., 2018). However, it
470 is possible that this effect could result from residual mtFAS activity, as complete knockout of the
471 mtFAS pathway proved impossible in this system. Furthermore, at least in the case of
472 UQCRFS1 and LYRM7, the maintenance of CIII may have been clonally selected for as cells
473 require CIII function for quinone oxidation and dihydroorotate dehydrogenase activity to make
474 uridine (Khutornenko et al., 2014; Khutornenko et al., 2010). Therefore, cells that lack CIII are
475 auxotrophic for orotate or uridine, and lack of these metabolites in the culture medium may have
476 provided selective pressure for clones that employ some mechanism to escape the mtFAS-
477 dependent regulation of CIII. In fact, it is tempting to speculate that assembly of CIII may be an
478 essential function of mtFAS in mammalian cells.

479 Finally, the question of why cells have evolutionarily maintained a parallel pathway for lipid
480 synthesis in mitochondria remains interesting, especially given recent research demonstrating
481 the transfer of lipids between endoplasmic reticulum, mitochondria, and various other

482 organelles, implying that the answer cannot simply be compartmentalization. Acetyl-CoA is the
483 nearly universal fuel of mitochondrial oxidative metabolism, being the convergence point of the
484 catabolism of carbohydrates, fatty acids, ketones and some amino acids. Acetyl-CoA is also the
485 common substrate of mtFAS and the TCA cycle, where it is broken down to produce the
486 reduced NADH and $FADH_2$ that fuel the electron transport chain. Thus, the interaction of acyl-
487 ACP with the LYRM proteins to facilitate ETC assembly has high potential to be a regulatory
488 mechanism whereby acetyl-CoA regulates its own catabolism (Kastaniotis et al., 2004; Kursu et
489 al., 2013; Van Vranken et al., 2018). In other words, as acetyl-CoA is the substrate for mtFAS, it
490 is required for ACP acylation, which in turn is required for interaction with and activation of
491 LYRM proteins and ETC assembly. The assembled ETC catalyzes the oxidation of NADH and
492 $FADH_2$, which drives the TCA cycle and consumption of acetyl-CoA. Thus, when acetyl-CoA is
493 low, ACP acylation is diminished, ETC assembly is blunted, TCA cycling slows, and acetyl-CoA
494 consumption falls. This hypothesis is supported by the observation that yeast with defects in
495 mitochondrial pyruvate metabolism exhibit blunted ACP acylation and impaired ETC assembly
496 (Van Vranken et al., 2018). This elegant regulatory cycle provides cells with a potential
497 mechanism to monitor acetyl-CoA substrate availability and adjust ETC complex levels
498 accordingly, avoiding situations where the ETC sits idle in the absense of substrate, and
499 reducing the attendant deleterious consequences, such as the production of reactive oxygen
500 species. Similarly, it could potentially allow cells to ramp up oxidative capacity in settings of
501 excess mitochondrial acetyl-CoA.
502 Human mutations in genes encoding enzymes of the mtFAS pathway are rare, but continue
503 to be discovered (Gorukmez et al., 2019; Heimer et al., 2016; Li et al., 2020). Intriguingly,
504 patients with *Mecr* mutations exhibit muscle weakness and we show herein that mtFAS
505 mutation interferes with the normal differentiation of cultured myoblasts (Figure 6). The
506 implications of these studies for the broader population remain to be seen, however. For
507 example, many age-related human diseases exhibit evidence of decreased mitochondrial

508 respiration, including frequent defects in OXPHOS complex assembly, suggesting the
509 interesting possibility that alterations in mtFAS might contribute to mitochondrial impairments in
510 human disease. The role(s) of mtFAS in aging and more prevalent diseases that also involve
511 mitochondrial pathologies such as diabetes, heart disease, and cancer are essentially
512 unstudied. One recent publication suggested that lipoylation of PDH and expression of *Oxsm*
513 may be decreased in some tissues in diabetic mice (Gao et al., 2019). This raises the intriguing
514 prospect that augmenting mtFAS pathway function could "boost" or rescue mitochondrial
515 oxidative metabolism in settings where mitochondrial respiration is sub-optimal. Recent studies
516 have shown enhancement of mitochondrial metabolism upon ACP overexpression, although the
517 molecular mechanisms and dependence of these phenotypes on mtFAS are unclear (Hou et al.,
518 2019; Zhang et al., 2019). It is therefore important to thoroughly examine how this pathway
519 functions both in normal biology and in disease settings. Understanding the rate limiting steps in
520 the cycle, its mode of regulation, and the mechanisms through which it can be manipulated
521 could one day allow mtFAS to be harnessed therapeutically to build better mitochondria and
522 treat metabolic disease.
523
524 **Materials and Methods**
525
526 ***Mcat*, *Oxsm*, and *Mecr* mutant cell lines**
527 C2C12 immortalized mouse skeletal myoblasts (ATCC CRL-1772) were grown in DMEM with
528 4.5 g/L glucose, glutamine, and sodium pyruvate (Corning, 10-013-CV) supplemented with 10%
529 FBS (Sigma, F0926) at 37°C in a humidified atmosphere containing 5% CO_2. To generate
530 mtFAS knockout clones, two guides per gene were designed targeting exon 1 or exon 2 of the
531 mouse *Mcat*, *Oxsm*, and *Mecr* genes (see key resources table for sequences) and cloned in the
532 pLentiCRISPR v2 vector. Parental C2C12 cells were transfected with
533 pLentiCRISPRv2_sgmtFAS or empty vector and 48 hours later the cells were sorted based on

534 GFP signal and plated in a 96-well plate to obtain single cell colonies. Colony number and size
535 was assessed by brightfield microscopy. Clones were screened based on MCAT, OXSM, and
536 MECR protein levels. Three *Oxsm* and *Mecr* mutant clones, three control clones, and two *Mcat*
537 mutant clones were ultimately selected for further experiments. For growth assays,
538 Quantification of single cell clone number and colony size 7 days after single cell sort. Small
539 clones = <150 cells, Med = 150-500 cells, Large = >500 cells. B. Cells were plated at 100,000
540 cells/plate in 10 cm dishes and counted every 24 hours.
541
542 **Stable FASN knockdown**
543 HEK293T cells were transiently transfected with pLKO.1 shFASN or scramble shRNA control
544 along with the lentiviral packaging plasmids psPAX2 and pMD2.G using polyethylenimine. 48
545 hours after transfection, viral supernatant was collected, filtered through a 0.45 µm
546 polyethersulfone membrane, and stored at 4°C. 10 µg/mL Polybrene (EMD Millipore, TR-1003-
547 G) was added and a 1:1 mixture of viral supernatant and fresh growth medium (DMEM +
548 10%FBS) was applied directly to *Oxsm* mutant cells, along with wild type C2C12 controls, and
549 incubated for 16 hours at 37°C in a humidified incubator with 5% CO_2. Viral media was
550 discarded and replaced with fresh growth media and cells were allowed to recover and expand
551 for 24 hours. After the recovery period, stably infected cells were selected with 2 µg/mL
552 puromycin for 1 week. Knockdown of FASN was confirmed via immunoblotting as described
553 below.
554
555 ***Lipt1* mutant cell lines**
556 C2C12 myoblasts were grown in DMEM High Glucose (Sigma, D5796) supplemented with 10%
557 FBS (Gemini Bio-Products #100-106) and penicillin/streptomycin (HyClone) at 37°C in a
558 humidified atmosphere containing 5% CO_2. To establish LIPT1 mutant clones, 2 guides were
559 designed targeting the coding region of the mouse *Lipt1* gene and cloned in the px459 vector.

560 Parental C2C12 cells were transfected with px459_sgLIPT1 or empty vector and three days
561 later the cells were sorted based on GFP signal. GFP positive cells were subsequently plated to
562 obtain single cell colonies and screened based on LIPT1 protein levels and lipoylation of
563 pyruvate dehydrogenase (PDH) and 2-oxoglutarate dehydrogenase (OGDH). Two *Lipt1* mutant
564 clones and one wild type clone were ultimately selected for further experiments.
565
566 **Crude mitochondrial isolation**
567 Cells were harvested by incubation with 0.25% trypsin-EDTA (Gibco, 25200-072), pelleted,
568 washed once with ice cold sterile PBS (Gibco, 10010-023), and frozen at -80°C. Upon thawing,
569 cells were resuspended in 1 mL CP-1 buffer (100mM KCl, 50mM Tris-HCl, 2mM EGTA, pH 7.4)
570 and mechanically lysed by 10 passes through a 27-gauge needle, and centrifuged at 700 x g to
571 pellet unlysed cells and debris. Supernatant was moved to a new tube and centrifuged at
572 10,000 x g to pellet crude mitochondrial fraction. Post-mitochondrial supernatant (PMS) was
573 saved for immunoblotting or discarded. Mitochondrial pellets were resuspended in a small
574 volume of CP-1 buffer equal to approximate pellet volume and used in assays described below.
575
576 **SDS-PAGE and Immunoblotting**
577 Whole cell lysates were prepared by scraping cells directly into Ripa buffer (50mM Tris-HCl, 1%
578 NP-40, 0.5% Na-Deoxycholate, 0.1% SDS, 150mM NaCl, 2mM EDTA) supplemented with
579 protease and phosphatase inhibitors (Sigma Aldrich P8340, Roche Molecular 04906845001),
580 incubated on ice for 45 minutes with vortexing every 5 min, and then centrifuged at 16,000 x g
581 for 10 minutes at 4°C to remove insoluble material. Supernatant was saved as whole cell lysate
582 (WCL). WCL, PMS, and/or crude mitochondrial fractions were normalized for total protein
583 content via BCA Assay (Thermo Scientific 23225). Samples were resolved by SDS-PAGE on
584 Tris-glycine gels (Invitrogen XP04205BOX) and transferred to nitrocellulose or PVDF
585 membranes. Immunoblotting was performed using the indicated primary antibodies which are

586 listed in the key resources table according to the manufacturers' recommendations, and
587 analyzed by Licor Odyssey.
588
589 **Blue Native-PAGE**
590 Crude mitochondrial fractions were isolated and normalized for total protein content as
591 described above. Blue Native (BN) PAGE was performed using the Invitrogen NativePAGE
592 system. 100 µg of mitochondria were pelleted at 10,000 x g for 10 minutes at 4°C and
593 resuspended in 1x pink lysis buffer (Invitrogen, BN20032). Digitonin (GoldBio D-180-2.5) was
594 added to a final concentration of 1% mass/volume. Samples were incubated on ice for 15
595 minutes, then spun for 20 minutes at 20,000 x g. 6 µL of NativePAGE sample buffer (Invitrogen,
596 BN20041) was added and 10 µL of sample was run on precast 3-12% NativePAGE gels
597 (Invitrogen, BN2011BX10) with NativePAGE anode buffer (Invitrogen, BN2001) and dark blue
598 cathode buffer (Invitrogen, BN2002) at 150 V for 1 hour then switched to light blue cathode
599 buffer (Invitrogen, BN2002) and run at 30 V overnight. Gels were subsequently transferred to
600 PVDF at 100 V, washed with methanol, and blotted with the indicated primary antibodies which
601 are listed in the key resources table according to the manufacturers' recommendations.
602 Secondary anti-mouse HRP antibody listed in the key resources table and SuperSignal West
603 Femto Maximum Sensitivity Substrate (Thermo, 34096) was used to visualize bands on film
604 (GeneMate, F-9024-8X10).
605
606 **Flux lipidomics**
607 Quadruplicate biological replicates of mtFAS mutant and control cells were plated at 35%
608 confluence in normal growth medium, then switched to labeling media (DMEM base (Corning,
609 17-207-CV), supplemented with 25 mM $U^{13}C$-glucose (Cambridge Isotopes, CLM-1396) and
610 4mM glutamine (Sigma G7513)) for 0, 0.25, 0.5, or 1 population doubling time. Samples were
611 harvested at 70% confluence via incubation with 0.25% trypsin (Gibco, 25200-072), and

612 pelleted at 300 x g for 5 minutes at 4°C, flash frozen in liquid nitrogen, and stored at -80°C.
613 Lipids were extracted from cell pellets in a randomized order using a solution of 225 µL
614 methanol (MeOH) containing internal standards (IS) (Avanti SPLASH LIPIDOMIX, 10 µL each /
615 sample) and 750 µL methyl tert-butyl ether (MTBE) (Matyash et al., 2008). The samples were
616 sonicated for 1 minute, rested on ice for 1 hour, briefly vortexed every 15 minutes then 188 µL
617 dd-H_2O was added to induce phase separation. All solutions were pre-chilled on ice. The
618 sample was then vortexed for 20 seconds, rested at room temperature for 10 minutes, and
619 centrifuged at 3,000 x g for 5 minutes at 4°C. The upper, organic phases were collected and
620 evaporated to dryness under vacuum. Lipid samples were reconstituted in 250 µL isopropyl
621 alcohol. Concurrently a process blank sample was brought forward as well as a pooled quality
622 control (QC) sample, prepared by taking equal volumes (~10 µL per sample) from each sample
623 after final resuspension. Lipid extracts were separated on a Waters Acquity UPLC CSH C18 1.7
624 µm 2.1 x 100 mm column maintained at 65 °C connected to an Agilent HiP 1290 Sampler,
625 Agilent 1290 Infinity pump and Agilent 6530 Accurate Mass Q-TOF dual AJS-ESI mass
626 spectrometer. For positive mode, the source gas temperature was set to 225 °C, with a drying
627 gas flow of 11 L/min, nebulizer pressure of 40 psig, sheath gas temp of 350 °C and sheath gas
628 flow of 11 L/min. VCap voltage was set at 3500 V, nozzle voltage 1000 V, fragmentor at 110 V,
629 skimmer at 85 V and octopole RF peak at 750 V. For negative mode, the source gas
630 temperature was set to 300 °C, with a drying gas flow of 11 L/min, a nebulizer pressure of 30
631 psig, sheath gas temp of 350 °C and sheath gas flow 11 L/min. VCap voltage was set at 3500
632 V, nozzle voltage 2000 V, fragmentor at 100 V, skimmer at 65 V and octopole RF peak at 750
633 V. Samples were analyzed in a randomized order in both positive and negative ionization
634 modes in separate experiments acquiring with the scan range *m/z* 100 – 1700. Mobile phase A
635 consists of ACN:H_2O (60:40 *v/v*) in 10 mM ammonium formate and 0.1% formic acid, and
636 mobile phase B consists of IPA:ACN:H_2O (90:9:1 *v/v*) in 10 mM ammonium formate and 0.1%
637 formic acid. The chromatography gradient for both positive and negative modes starts at 15%

638 mobile phase B then increases to 30% B over 2.4 minutes, it then increases to 48% B from 2.4
639 – 3.0 minutes, then increases to 82% B from 3 – 13.2 minutes, then increases to 99% B from
640 13.2 – 13.8 min where it was held until 16.7 minutes and then returned to the initial conditions
641 and equilibrated for 5 minutes. Flow was 0.4 mL/min throughout, injection volume was 3 µL for
642 positive and 10 µL negative mode. Tandem mass spectrometry was conducted using the same
643 LC gradient at collision energy of 25 V. QC samples (n=8) and blanks (n=4) were injected
644 throughout the sample queue and ensure the reliability of acquired data. Results from LC-MS
645 experiments were collected using Agilent Mass Hunter (MH) Workstation and analyzed using
646 the software packages MH Qual, MH Quant, and Lipid Annotator (Agilent Technologies, Inc.).
647
648 **FAMES fluxomics**
649 Lipid extracts were saponified by an addition of 1 mL of 5% HCl in MeOH. Samples were
650 vortexed for 15 seconds then placed into a sand bath heated at 80°C for 2 hours. The resulting
651 methanolysis reaction products were extracted with hexanes (3 X 1 mL) by vortexing for 15
652 seconds and then centrifuged for 4 minutes at 10,000 x g. Supernatants were transferred to new
653 tubes and gently dried under a nitrogen stream at room temperature. Samples were
654 resuspended in 200 µL EtOAc and transferred to GC-MS vials with insert. GC-MS analysis was
655 performed with an Agilent 5977b GC-MS HES-MSD and an Agilent 7693A automatic liquid
656 sampler. Samples were injected (1 µL) 10:1, with an inlet temperature of 250°C. The gas
657 chromatograph had an initial temperature of 67°C for one minute followed by a 50°C/min ramp
658 to 197°C, a second ramp of 10°C/minute up to 325°C began immediately with a hold time of 2
659 minutes. A 30-meter Agilent Zorbax DB-5MS with 10 m Duraguard capillary column was
660 employed for chromatographic separation. Helium was used as the carrier gas at a rate of 1
661 mL/minute. A gain of 5.0 was used for data acquisition. High Efficiency Source and quadrupole
662 temperatures were held at 275 °C and 190 °C, respectively.

663 **Kinetics (Fluxomics) Calculation**

664 Target compounds were fed to the emass software created by the Rockwood group (Rockwood
665 and Haimi, 2006). This software calculated masses and relative abundances for all isotopes
666 observed so if for one compound only M2 was observed and another went out to M5, emass
667 would calculate M0-M2 for compound 1 and M0-M5 for compound 2. Matrixes of the theoretical
668 isotopic abundances and the measured isotopic abundances were created. The multiplicative
669 inverse of each matrix was calculated and then the dot product of the theoretical inverse matrix
670 and the measured inverse matrix was calculated. The data from one row of the resulting matrix
671 (all rows are identical) is then sum normalized. In an unlabeled sample M0 will be measured as
672 1 and all other isotopes should be 0 (standard Metabolomic Flux Analysis).

673 **Cytochrome *bc₁* complex (CIII) and Citrate Synthase (CS) Activity Assays**

674 CIII and CS activities were measured following the protocol published in (Spinazzi et al., 2012).
675 For CIII activity assay, 10 µg of purified mitochondria was mixed in 990 µL of the assay buffer
676 (25 mM potassium phosphate (pH 7.5), 75 µM oxidized cytochrome c, 500 µM KCN, 100 µM
677 EDTA (pH 7.5), 0.025% (volume/volume) Tween-20). After the baseline reading at 550 nM for 2
678 min, the reaction was started by adding 10 µl of 10 mM decylubiquinol and the increasing
679 absorbance at 550 nm was measured for the next 3 min. In parallel CIII-independent
680 cytochrome c reduction was measured by adding antimycin A in a separate reaction mixture
681 and subtracted from the reaction without antimycin A. CIII activity was calculated and expressed
682 as nmole/min/mg. CS activity was measured by incubating 5 µg of purified mitochondria in 950
683 µL of the assay buffer (100 mM Tris (pH 8.0), 0.1% (volume/volume) Triton X-100, 100 µM
684 DTNB (5,5'-dithiobis(2-nitrobenzoic acid)), 300 µM Acetyl CoA). After reading the baseline
685 activity at 412 nm for 2min, the reaction was started by adding 50 µL of 10 mM oxaloacetic acid
686 (OA) and monitored the increase in the absorbance at 412 nm for 3 min. CS activity was

687 calculated by subtracting the baseline increase at 412 nm from the increase after addition of OA
688 and expressed as nmole/min/mg.
689
690 **Seahorse Experiments**
691 Seahorse experiments were performed on a Seahorse XFe96 Analyzer. Cells from n=2 clones
692 (Mcat mutants) or n=3 clones (Oxsm, Mecr mutants and controls) were plated in 8 wells of a 96-
693 well seahorse plate at a density of 6,000 cells/well in DMEM + 10% FBS. The morning of the
694 experiment, cells were washed 2x and then media was replaced with DMEM (Sigma D5030)
695 supplemented with 25mM glucose, 2mM glutamine and 1mM pyruvate, pH 7.4. A standard
696 mitochondrial stress test was performed using 1μM oligomycin, 3μM FCCP, and 0.5 μM
697 Rotenone + 0.5μM Antimycin A. Assay protocol was standard (3 measurements per phase,
698 acute injection followed by 3 min mixing, 0 min waiting, and 3 min measuring). Data were
699 normalized to total cellular protein per well (Thermo BCA Kit cat. 23225). Results were analyzed
700 in WAVE software and processed through the XF Mito Stress Test Report.
701
702 **Mitochondrial membrane potential microscopy and quantitation**
703 Cells were plated in chambered coverglass (Fisher, 155409) and allowed to adhere overnight.
704 Media was changed and replaced with fresh DMEM + 10% FBS containing 25 nM MitoTracker
705 Red CMXROS and 50 nM MitoTracker Green (Invitrogen M7512 and M7514). Cells were
706 incubated with dyes for 30 minutes at 37°C in a humidified incubator with 5% CO2, then washed
707 twice and replaced with fresh media, and imaged using a Zeiss AxioObserver Z1 fluorescence
708 microscope (Carl Zeiss) equipped with 40x oil-immersion objective. Digital fluorescence and
709 differential interference contrast (DIC) images were acquired using a monochrome digital
710 camera (AxioCam 506, Carl Zeiss). Images were exported from Zeiss Zen software package
711 and analyzed for fluorescence intensity using FiJi ImageJ. Images are representative of n≥38
712 images from two clones imaged in two independent experiments.

713

714 **Co-immunoprecipitation of ACP-Flag and LYRM-V5 proteins**

715 10cm plates of HEK293T cells were transiently transfected with 10 µg of total DNA using
716 Lipofectamine 2000 (Invitrogen, 11668019). DNA was made up of equal amounts of empty
717 vector, pcDNA3.1 hNDUFAB1-Flag, and pcDNA3.1 LYRM-V5 constructs alone or in
718 combination as indicated. 48 hours after transfection, cells were collected by incubation with
719 0.25% trypsin, washed, and pelleted at 300g. Crude mitochondria were isolated as described
720 above and protein content was assessed via BCA assay. 500 µg of crude isolated mitochondria
721 were pelleted and resuspended in 500 µL of XWA buffer (20 mM HEPES, 10 mM KCl, 1.5 mM
722 MgCl2, 1 mM EDTA, 1 mM EGTA, 150 mM NaCl, 2.1 mg/mL NaF, 10.8 mg/mL β-
723 glycerophosphate, pH 7.4) then lysed by incubation in 0.7% digitonin for 30 minutes rotating at
724 4°C. Insoluble material was removed by centrifugation at 20,000g for 20 minutes, and
725 supernatant was incubated with 20 µL anti-Flag agarose beads (Sigma, F2426) for 2 hours
726 rotating at 4°C. Beads were washed 3 times with XWA buffer and samples were eluted in 40 µL
727 of 1x Lamelli buffer (10% glycerol, 50 mM Tris HCl, pH 6.8, 1% SDS) for 10 minutes at 65°C.
728 Samples were loaded on Tris-Glycine gels, separated by SDS-PAGE, and immunoblotted for
729 Flag and V5 as described above. Results are representative of three separate experiments.

730

731 **Quantitative proteomics**

732 Duplicate biological samples of two control clones, two *Oxsm* mutant clones, and two *Mecr*
733 mutant clones were grown in standard proliferative conditions to 70% confluence and harvested
734 by incubation with 0.25% trypsin, pelleted at 300 g, washed with sterile PBS, flash frozen in
735 liquid nitrogen and stored at -80°C. As only eleven samples could be run with the SL-TMT
736 protocol, one *Oxsm* clone had only one sample analyzed and was ultimately omitted from the
737 results.

738 *Protein extraction, digestion, and TMT labeling.* Samples were processed using the SL-TMT
739 protocol as described previously (Navarrete-Perea et al., 2018). Specifically, mitochondrial
740 pellets were resuspended in 200 µL of lysis buffer (8M urea, 200mM EPPS pH 8.5 plus 1X
741 cOmplete protease and phosphatase inhibitor) and syringe lysed (10 times with 21-gauge
742 needle). Following a BCA assay to estimate protein concentration, all lysates were reduced (20
743 min with 5mM TCEP at room temperature), alkylated (20 min with 10mM iodoacetamide, at
744 room temperature in the dark), and quenched (20 min with 10mM DTT, at room temperature in
745 the dark). Proteins were precipitated by chloroform methanol precipitation, as described
746 previously (Paulo and Gygi, 2015). Precipitated proteins were resuspended in 200mM EPPS pH
747 8.5 (~1mg/ml) and digested first with LysC (Wako) for 3 hours at 37°C shaking on a vortexer
748 (speed =50%) followed by a 6 hour trypsin digestion at 37°C (sequencing grade, Pierce). Both
749 enzymes were added in the presence of beads and at a 1:100 protease-to-peptide ratio.
750 Following digestion, the samples were centrifuged as above and held to the magnet for 2 min.
751 Digested peptides were simply transferred into a new tube. The beads were then washed with
752 50 µL of 0.2M EPPS pH8.5, which was combined with the initial elution. We added a final
753 volume of 30% acetonitrile to the eluted peptides and labelled the 50 µg of peptide with 100 µg
754 of TMT directly into the digestion mixture. To check mixing ratios, 2 µg of each sample were
755 pooled, desalted, and analyzed by mass spectrometry. Using normalization factors calculated
756 from this "label check," samples were mixed 1:1 across all 11 channels and desalted using a 50
757 mg Sep-Pak solid phase extraction column. The approximately 300 µg of peptide were
758 fractionated with basic pH reversed-phase (BPRP) HPLC, collected in a 96-well plate and
759 combined down to 24 fractions prior to desalting and subsequent LC-MS/MS processing (Paulo,
760 2014; Paulo and Gygi, 2017).
761 *Mass spectrometry analysis.* Mass spectrometric data were collected on an Orbitrap Fusion
762 mass spectrometer coupled to a Proxeon NanoLC-1000 UHPLC. The 100 µm capillary column
763 was packed with 35 cm of Accucore 150 resin (2.6 µm, 150Å; ThermoFisher Scientific). The

764 SPS-MS3 method use used to reduce ion interferences that may result in ratio compression
765 (Gygi et al., 2019; Paulo et al., 2016). Peptides in each fraction were separated using a 150 min
766 gradient from ~5 to 35% acetonitrile. The scan sequence began with an MS1 spectrum
767 (Orbitrap analysis, resolution 120,000, 350−1400 Th, automatic gain control (AGC) target 5E5,
768 maximum injection time 100 ms). The top ten precursors were then selected for MS2/MS3
769 analysis. MS2 analysis consisted of collision-induced dissociation (CID), quadrupole ion trap
770 analysis, automatic gain control (AGC) 2E4, NCE (normalized collision energy) 35, q-value 0.25,
771 maximum injection time 120 ms), and isolation window at 0.7. Following acquisition of each
772 MS2 spectrum, we collected an MS3 spectrum in which multiple MS2 fragment ions are
773 captured in the MS3 precursor population using isolation waveforms with multiple frequency
774 notches. MS3 precursors were fragmented by HCD and analyzed using the Orbitrap (NCE 65,
775 AGC 1.5E5, maximum injection time 150 ms, resolution was 50,000 at 400 Th). Spectra were
776 converted to mzXML via MSconvert (Chambers et al., 2012). Database searching included all
777 entries from the Mus musculus Database (UniProt; August 2017). The database was
778 concatenated with one composed of all protein sequences for that database in the reversed
779 order. Searches were performed using a 50-ppm precursor ion tolerance for total protein level
780 profiling. The product ion tolerance was set to 0.9 Da. These wide mass tolerance windows
781 were chosen to maximize sensitivity in conjunction with SEQUEST searches and linear
782 discriminant analysis (Beausoleil et al., 2006; Huttlin et al., 2010). TMT tags on lysine residues
783 and peptide N termini (+229.163 Da) and carbamidomethylation of cysteine residues (+57.021
784 Da) were set as static modifications, while oxidation of methionine residues (+15.995 Da) was
785 set as a variable modification. Peptide-spectrum matches (PSMs) were adjusted to a 1% false
786 discovery rate (FDR) (Elias and Gygi, 2007, 2010). PSM filtering was performed using a linear
787 discriminant analysis, as described previously (Huttlin et al., 2010) and then assembled further
788 to a final protein-level FDR of 1% (Elias and Gygi, 2007). Proteins were quantified by summing
789 reporter ion counts across all matching PSMs, also as described previously (McAlister et al.,

790 2012). Reporter ion intensities were adjusted to correct for the isotopic impurities of the different
791 TMT reagents according to manufacturer specifications. The signal-to-noise (S/N)
792 measurements of peptides assigned to each protein were summed and these values were
793 normalized so that the sum of the signal for all proteins in each channel was equivalent to
794 account for equal protein loading. Finally, each protein abundance measurement was scaled,
795 such that the summed signal-to-noise for that protein across all channels equals 100, thereby
796 generating a relative abundance (RA) measurement.

797 Technical replicates from the geometric mean-normalized proteomics data were averaged.
798 Heatmaps were generated by calculating the average value for the GFP replicates and dividing
799 each replicate (experimental and control) by this value for each protein. A list of ETC component
800 proteins was passed into the xpressplot.heatmap() function from XPRESSplot (Berg et al.,
801 2020; Waskom, 2018) and further formatting was performed using Matplotlib (Hunter, 2007).
802 The volcano plot for the Mecr vs GFP proteomics data was generating by providing lists of
803 Mitocarta (Calvo et al., 2016; Pagliarini et al., 2008) and ETC proteins and the technical-
804 replicate, geometric-normalized dataframe for both GFP and Mecr replicates to the
805 xpressplot.volcano() function (Berg et al., 2020).

806 ***Lipt1* KO Seahorse Experiments**

807 Seahorse experiments were performed on a Seahorse XFe96 Analyzer. Cells were plated at a
808 density of 10,000 cells/well in DMEM + 10% FBS. The morning of the experiment, cells were
809 washed 2x and then media was replaced with Seahorse media: DMEM (Sigma D5030)
810 supplemented with 10mM glucose, 2mM glutamine and 1mM pyruvate, pH 7.4. A standard
811 mitochondrial stress test was performed using 2μM oligomycin, 1μM Carbonyl cyanide m-
812 chlorophenyl hydrazone (CCCP), and then 1μM Antimycin A. Assay protocol was standard (3
813 measurements per phase, acute injection followed by 3 min mixing, 0 min waiting, and 3 min

814 measuring). Data were normalized to 10,000 cells/well. Results were analyzed in WAVE
815 software and processed through the XF Mito Stress Test Report.
816
817 **Glutamine Tracing Experiments**
818 C2C12 cells were plated in a 60mm plate at a density of 100,000 cells/plate. The following day,
819 media was changed to tracing media: DMEM (Sigma 5030) supplemented with 2.5mM glucose,
820 4mM [U-^{13}C]glutamine, 1mM pyruvate, and 5% dialyzed FBS. Cells were harvested 24 hours
821 later by washing once with ice-cold normal saline and then quenched with 800 µL 80:20
822 methanol:water. Methanol lysates were then subjected to three rapid freeze-thaw cycle and then
823 spun at 16,000 x g for 10 minutes at 4°C. The supernatants, with 1µL d27-myristic acid added
824 (Sigma 68698) (GCMS only) as an internal control, were evaporated using a SpeedVac
825 concentrator.
826
827 **Liquid Chromatography Mass Spectrometry (LCMS)**
828 A replicate plate was set up during tracing experiments to assess relative metabolite
829 concentrations using LCMS and harvested as described above. Dried metabolites were
830 reconstituted in 100 µl of 0.03% formic acid in analytical-grade water, vortexed and centrifuged
831 to remove insoluble material. The supernatant was collected and subjected to targeted
832 metabolomics analysis as described on an AB SCIEX QTRAP 5500 liquid chromatography/triple
833 quadrupole mass spectrometer (Applied Biosystems SCIEX) (Kim et al., 2000). The injection
834 volume was 20 µl. Chromatogram review and peak area integration were performed using
835 MultiQuant (version 2.1, Applied Biosystems SCIEX). The peak area for each detected
836 metabolite was normalized against the total ion count of that sample.
837
838 **Gas Chromatography Mass Spectrometry (GCMS) derivatization**

839 The supernatants, with 1μL d27-myristic acid added as an internal control, were evaporated
840 using a speed vac. Dried metabolites were re-suspended in 30μL anhydrous pyridine with
841 10mg/mL methoxyamine hydrochloride and incubated at room temperature overnight. The
842 following morning, the samples were cooked at 70°C for 10-15min and then centrifuged at
843 16,000 x g for 10min. The supernatant was transferred to a pre-prepared GC/MS autoinjector
844 vial containing 70μL N-(tert-butyldimethylsilyl)-N-methyltrifluoroacetamide (MTBSTFA)
845 derivatization reagent. The samples were incubated at 70°C for 1 hour following which aliquots
846 of 1μL were injected for analysis. Samples were analyzed using either an Agilent 6890 or 7890
847 gas chromatograph coupled to an Agilent 5973N or 5975C Mass Selective Detector,
848 respectively. The observed distributions of mass isotopologues were corrected for natural
849 abundance.
850
851 **C2C12 differentiation experiments**
852 MtFAS mutants and controls were seeded in 10 cm plates and grown in DMEM (Corning, 10-
853 013-CV) supplemented with 10% FBS (Sigma, F0926) to 70% confluency (Day -1). The next
854 day at 95% confluency cells were switched to DMEM supplemented with 2% horse serum
855 (Thermo, 16050122)(Day 0). For the next 7 days, media was changed and replaced with fresh
856 DMEM + 2% horse serum every 24 hours. Samples were imaged via brightfield microscopy or
857 harvested for immunoblotting or RNAseq experiments at the indicated time points after
858 switching to differentiation medium.
859
860 **RNA-Seq**
861 *RNA isolation and quality assessment:* Four replicates of each genotype (GFP, *Mcat*, *Oxsm,*
862 and *Mecr* mutants) were grown and harvested at Day -1, Day 0, and Day 1 of the differentiation
863 time course as described above —with the exception of GFP Day 0, which only had three
864 replicates. Total RNA was extracted from one confluent 10 cm dish per replicate using TRI

865 Reagent (Zymo Research, R2050-1-200) according to the manufacturer's protocol. Briefly, cells
866 were homogenized in 1 ml of TRI reagent for 5 mins. After addition of 0.2 mL of chloroform, the
867 homogenate was shaken vigorously for 15 s, allowed to stand for 15 mins at RT and centrifuged
868 at 12,000xg for 15 min at 4°C. The aqueous phase was mixed with 0.5 mL of 2-propanol and 10
869 µg of glycogen (Thermo Scientific, R0561) and RNA was precipitated overnight in -20°C. The
870 precipitated RNA was pelleted at 15,000xg for 30 min at 4°C, washed with 1 mL of 75% EtOH
871 and dissolved in nuclease-free water. RNA quantity and purity were assessed using the
872 NanoDrop One spectrophotometer (Thermo Fisher) and RNA integrity was assessed using the
873 Agilent RNA ScreenTape Assay.
874 Illumina TruSeq Stranded mRNA Library Prep (RIN 8-10) with UDI: Intact poly(A) RNA was
875 purified from total RNA samples (100-500 ng) with oligo(dT) magnetic beads and stranded
876 mRNA sequencing libraries were prepared as described using the Illumina TruSeq Stranded
877 mRNA Library Prep kit (20020595) and TruSeq RNA UD Indexes (20022371). Purified libraries
878 were qualified on an Agilent Technologies 2200 TapeStation using a D1000 ScreenTape assay
879 (cat# 5067-5582 and 5067-5583). The molarity of adapter-modified molecules was defined by
880 quantitative PCR using the Kapa Biosystems Kapa Library Quant Kit (cat#KK4824). Individual
881 libraries were normalized to 1.30 nM in preparation for Illumina sequence analysis. NovaSeq 2 x
882 50 bp Sequencing: Sequencing libraries (1.3 nM) were chemically denatured and applied to an
883 Illumina NovaSeq flow cell using the NovaSeq XP chemistry workflow (20021664). Following
884 transfer of the flowcell to an Illumina NovaSeq instrument, a 2 x 51 cycle paired end sequence
885 run was performed using a NovaSeq S1 reagent Kit (20027465). Data Analysis: Reads were
886 trimmed of adaptor sequence using cutadapt (v.2.8)(Martin, 2011). Trimmed reads were aligned
887 to the mouse genome (mm10) using STAR (v.2.5)(Dobin et al., 2013) with the parameters '--
888 outFilterMismatchNoverLmax 0.2 --sjdbOverhang 49 --outReadsUnmapped Fastx --outSAMtype
889 BAM SortedByCoordinate --quantMode GeneCounts' and with '–sjdbGTFfile' supplied with
890 transcript annotations from Ensembl (Mus_musculus.GRCm38.99.chr_patch_hapl_scaff.gtf).

Three samples were censored from further analyses (one replicate each of GFP day minus one, Mcat day zero, and Oxsm day one) due to outlier status relative to all remaining samples. Differential expression was determined using DESeq2 (v.1.26.0)(Love et al., 2014). Count data were shrunk using the 'apeglm' option of the DESeq2 function 'lfcShrink'.

Quantification and Statistical Analyses

For flux lipidomics and metabolomics, mitoTracker quantification, and Seahorse cellular respiration, statistically significant differences were determined using GraphPad Prism 8. Data were analyzed by one-way or two-way Anova as appropriate followed by Dunnett's multiple comparison test (when compared only to control) or Tukey's multiple comparison test (when comparing all groups, such as for lipid isotopologue analysis). A p-value of 0.05 was considered to be statistically significant. For RNAseq and quantitative proteomics, analyses are described in the corresponding sections.

Author Contributions:

Conceptualization, S.M.N. and J.R.; Methodology, S.M.N., A.S., S.F.R., J.A.P., J.A.M., J.E.C., S.P.G., R.J.D., and J.R.; Investigation, S.M.N., A.S., S.F.R., C.L.B., S.F., S.L., Y.O. and M.J.; Formal Analysis, S.M.N., A.S., J.A.M, B.C.N., J.A.B., and J.T.M.; Visualization, S.M.N., J.A.B., and J.T.M.; Writing – Original draft, S.M.N.; Writing – Review & Editing, S.M.N., A.S., S.F., C.L.B., J.T.M., D.R.W., R.J.D., and J.R.; Resources, K.F., S.P.G., R.J.D., J.R.; Supervision, K.F., S.P.G., D.R.W., J.R.; Funding Acquisition, D.R.W., J.R.

Acknowledgements:

916 The authors are grateful to members of the Department of Biochemistry at the University of
917 Utah for useful discussion and feedback, specifically Chintan Kikani, Gabrielle Kardon, and
918 Dana Carroll. Cloning of CRISPR plasmids was done by the Mutation Generation and Detection
919 Core at the University of Utah. FACS to generate single cell clones was done in the Flow
920 Cytometry Core at the University of Utah. Flux lipidomics and analysis was performed at the
921 Metabolomics Core Facility at the University of Utah. RNA-Seq library preparation and
922 sequencing was performed by the High-Throughput Genomics Shared Resource at the
923 Huntsman Cancer Institute. This study was supported by grants from the NIH (GM115174 and
924 GM115129 to J.R.) and the Nora Eccles Treadwell Foundation (to J.R.), as well as HHMI (J.R.).
925 Support for SMN was also provided by UMDF and ACS postdoctoral fellowships, along with
926 T32HL007576. J.A.B. received support from NIDDK T32DK11096601 to Wendy W. Chapman
927 and Simon J. Fisher. R.J.D. is an advisor for Agios Pharmaceuticals and is supported by HHMI,
928 NCI (R35CA22044901) and the Once Upon a Time Foundation. A.S. is funded by NICHD
929 (F32HD096786). K.F. is funded by R01DK107397 and R21AG063077. J.E.C. is funded by
930 S10OD016232, S10OD021505, and U54DK110858. J.A.P. is funded by NIH/NIGMS grant R01
931 GM132129 and S.P.G. is funded by GM97645. The content is solely the responsibility of the
932 authors and does not necessarily represent the official views of the National Institutes of Health.
933
934 The authors declare no competing interests.
935
936 **Figure Legends**
937
938 **Figure 1: MtFAS is an essential pathway in mammalian skeletal myoblasts but does not**
939 **contribute to synthesis of major cellular lipids**. A. Schematic of the mitochondrial fatty acid
940 synthesis pathway and downstream lipoic acid synthesis. B. Crude isolated mitochondrial
941 fractions from duplicate single cell clones of *Mcat*, *Oxsm*, and *Mecr* mutants, compared with

942 GFP control clonal cell lines, were separated via SDS-PAGE and immunoblotted for the
943 indicated targets. * = Lipoic acid band (reprobe of earlier blot). # = non-specific bands C. Whole
944 cell lysates from stable cell lines generated by infecting *Oxsm* mutant cells (OxsmΔ) or GFP
945 controls with shRNA constructs targeting *FASN* (shFASN) or scramble control (shScramble)
946 were separated by SDS-PAGE and immunoblotted for FASN or tubulin. D.-E. Stable cell lines
947 created in (C.) were incubated with $U^{13}C$-glucose for the indicated number of doublings,
948 harvested, lipids extracted, and analyzed via LC-MS. Shown are quantitation of m+2
949 isotopologues for two representative phospholipid species, PC 16:0_16:0 and PC 16:0_18:0. †
950 = $p<0.001$, ‡ = $p<0.0001$, error bars are SEM.
951
952 **Figure 2: MtFAS mutants display profound loss of mitochondrial respiration and ETC**
953 **complexes.** A. Cells from three clones of each of the indicated genotypes were seeded in eight
954 wells of a 96-well seahorse plate and allowed to adhere overnight, then equilibrated and treated
955 with the indicated drugs following standard mitochondrial stress test protocols from the
956 manufacturer to determine Oxygen Consumption Rate (OCR). # = $p<0.01$, † = $p<0.001$, ‡ =
957 $p<0.0001$ all comparisons are to GFP control, error bars are SEM. B. Cells of the indicated
958 genotype were seeded in chambered coverglass slides, stained with Mitotracker Red and
959 Mitotracker Green, and imaged. C. Ratio of MitoTracker Red to MitoTracker Green fluorescence
960 of cells from 30 fields of view quantified using Fiji ImageJ. * = $p<0.05$, † = $p<0.001$, ‡ =
961 $p<0.0001$ all comparisons are to GFP control, error bars are SD. D. Mitochondrial lysates
962 generated from the indicated cell lines were normalized for total protein by BCA assay,
963 incubated with 1% digitonin, then separated by blue-native PAGE and immunoblotted with the
964 indicated antibodies.
965
966 **Figure 3: Posttranslational loss of ETC components in mtFAS mutants is specific to LYR**
967 **proteins and their targets.** A.-B. Duplicate samples from the indicated cell lines were grown

968 under proliferative conditions and subjected to TMT labeling and quantitative proteomics
969 analysis. A. Volcano plot of compiled Mecr clones vs. GFP controls showing all proteins (gray),
970 mitochondrial proteins (blue), and electron transport chain subunits (ETC, red). Dashed gray
971 lines indicate cutoffs for significance at -log10(p-value) = 1.3 and log2(Fold Change) = .59. B.
972 Heatmap depicting $\log_2$(Fold Change) of OXPHOS subunits in the indicated cell lines. C.
973 Quadruplicate samples from mtFAS mutant cells and controls were grown under proliferative
974 conditions. Total RNA was isolated, used as input for for mRNA library prep, and sequenced.
975 Resulting data were aligned to the mouse genome and analyzed for differential expression. ETC
976 subunit-encoding transcripts are shown in red vs. all other transcripts (gray). D.-G. Relative
977 abundance of the indicated LYR proteins or their targets in the indicated cell lines from the
978 quantitative proteomics experiment described in A.-B. # = $p<0.01$, † = $p<0.001$, ‡ = $p<0.0001$,
979 error bars are SD. All statistical comparisons shown are between mtFAS mutants and GFP-1
980 clone; p-values when compared with GFP-2 clone were similar or smaller than when compared
981 with GFP-1 clone. H. Crude mitochondrial lysates generated from the indicated cell lines by
982 differential centrifugation were normalized for total protein by BCA assay, separated by SDS-
983 PAGE, and immunoblotted with the indicated antibodies.
984
985 **Figure 4: Impairment of mtFAS promotes switch from oxidative to reductive**
986 **mitochondrial metabolism.** A.–E. Triplicate biological samples from mtFAS mutant cell lines or
987 GFP control were grown under standard proliferative conditions in high glucose media (25mM)
988 and harvested for steady-state metabolomics analysis by LC-MS. Shown are relative pool sizes
989 for the indicated metabolites. * = $p<0.05$, # = $p<0.01$, † = $p<0.001$, ‡ = $p<0.0001$, error bars are
990 SD. F. Schematic of isotopomeric labeling of TCA cycle intermediates upon feeding with $U^{13}C$-
991 glutamine. Black circles indicate ^{13}C carbons derived from labeled glutamine via oxidative TCA
992 cycle flux (left). Purple circles indicate ^{13}C carbons derived from labeled glutamine via reductive
993 carboxylation (right). G.-L. Triplicate biological samples of the indicated genotype were labeled

994 for 24 hours with $U^{13}C$-glutamine, harvested, and analyzed via GC-MS for the indicated
995 metabolites and their isotopologues. * = p<0.05, # = p<0.01, † = p<0.001, ‡ = p<0.0001, error
996 bars are SD.
997
998 **Figure 5: MtFAS mutant phenotypes are not recapitulated by loss of lipoic acid alone.** A.
999 Immunoblot for the indicated proteins in whole cell lysates from Lipt1 mutant and control cell
1000 lines. B. In triplicate experiments, cells of each of the indicated clones were seeded in eight
1001 wells of a 96-well seahorse plate and allowed to adhere overnight, then equilibrated and treated
1002 with the indicated drugs following standard mitochondrial stress test protocols from the
1003 manufacturer to determine Oxygen Consumption Rate (OCR). # = p<0.01, † = p<0.001, ‡ =
1004 p<0.0001 all comparisons are to GFP control, error bars are SEM. C. Mitochondrial lysates
1005 generated from the indicated cell lines by differential centrifugation were normalized for total
1006 protein by BCA assay, incubated with 1% digitonin, then separated by BN-PAGE and
1007 immunoblotted with the indicated antibodies. D. Four biological replicates from mtFAS mutant
1008 cell lines or GFP control were grown under standard proliferative conditions and harvested for
1009 steady-state metabolomics analysis by LC-MS. Shown are relative pool sizes for the indicated
1010 metabolites. * = p<0.05, error bars are SD. E. Four biological samples of the indicated genotype
1011 were labeled for 24 hours with $U^{13}C$glutamine, harvested, and analyzed via GC-MS for the
1012 indicated metabolites and their isotopologues. * = p<0.05, # = p<0.01, † = p<0.001, error bars
1013 are SD.
1014
1015 **Figure 6: MtFAS is required for skeletal myoblast differentiation.** A. Volcano plot of
1016 quantitative proteomics experiment showing Mecr mutant samples (n=4) vs. GFP (n=4) controls;
1017 all proteins (gray), and proteins associated with the differentiated skeletal muscle lineage (red).
1018 Dashed lines indicate cutoffs for significance at $-\log_{10}$(p-value) = 1.3 and $\log_2$(Fold Change) =
1019 .59. B.-C. Cells of the indicated genotypes were plated and grown for 24 hours under

1020 proliferative conditions (day -1), then switched to 2% horse serum differentiation medium at 95%
1021 confluency (day 0). Medium was replaced daily for the indicated number of days. Plates were
1022 imaged (B) or whole cell lysates were collected at the indicated time points, separated by SDS-
1023 PAGE, and immunoblotted for the indicated proteins (C). D.-E. Quadruplicate samples from
1024 mtFAS mutant cells and controls were grown under proliferative conditions to 95% confluency
1025 then switched to 2% horse serum differentiation medium for 24 hours. Total RNA was isolated,
1026 used as input for mRNA library prep, and sequenced. Resulting data were aligned to the mouse
1027 genome and analyzed for differential expression. Transcripts for differentiation related proteins
1028 from panel (A) are shown in purple vs. all other transcripts (gray). F. Relative steady state pool
1029 sizes of the indicated metabolites in mtFAS mutant cell lines vs. GFP controls grown in
1030 proliferative conditions from steady-state LC-MS metabolomics analysis. * = $p<0.05$, # = $p<0.01$,
1031 † = $p<0.001$, ‡ = $p<0.0001$, error bars are SD.
1032
1033 **Supplementary Figure Legends**
1034
1035 **Figure supplement 1: mtFAS is required for growth of cultured skeletal myoblasts but**
1036 **does not significantly contribute to cellular fatty acids.** A. Quantification of single cell clone
1037 colony size 7 days after single cell sort. Small clones = <150 cells, Med = 150-500 cells, Large =
1038 >500 cells. B. Cells were plated at 100,000 cells/plate in 10 cm dishes and counted every 24
1039 hours. # = $p<0.01$, all groups compared with control, † = $p<0.001$, all groups compared with
1040 control, error bars SEM. C. Sub-cellular fractionation of Mecr mutant cell lines and control.
1041 Whole cell lysate (WCL), post mitochondrial supernatant (PMS), and mitochondrial lysate (Mito)
1042 was isolated from each cell line indicated, normalized for total protein via BCA assay, and
1043 immunoblotted for Mecr or VDAC as a mitochondrial marker control. D. Control (GFP) or Oxsm
1044 mutant (OxsmΔ) cells were stably infected with shRNA targeting FASN (shFASN) or control
1045 (shScramble) then incubated with $U^{13}C$-glucose for one doubling were harvested, lipids

1046 extracted and saponified, and analyzed via FAMES analysis. Shown are quantitation of c16:0
1047 and c18:0 fatty acids. ns = non-significant, * = p<0.05, # = p<0.01, † = p<0.001, error bars are
1048 SEM.
1049
1050 **Figure supplement 2: ETC complex assembly and activity is regulated by interaction of**
1051 **LYRM proteins with ACP.** A. Cells from three clones of each of the indicated genotypes were
1052 seeded in eight wells of a 96-well seahorse plate and allowed to adhere overnight, then
1053 equilibrated and treated with the indicated drugs following standard mitochondrial stress test
1054 protocols from the manufacturer to determine ExtraCellular Acidification Rate (ECAR). B. Cells
1055 of the indicated genotype were seeded in chambered coverglass slides, stained with Mitotracker
1056 Red and Mitotracker Green, and imaged. Fluorescence of cells from 30 fields of view was
1057 quantified using Fiji ImageJ. * = p<0.05, † = p<0.001, ‡ = p<0.0001 all comparisons are to GFP
1058 control, error bars are SD. C. Crude mitochondrial fractions were isolated from triplicate
1059 biological samples of mtFAS mutant and control cells using differential centrifugation. Isolated
1060 mitochondria were normalized for protein content via BCA assay and analyzed for Bc1-complex
1061 activity and citrate synthase activity (CS). ns = non-significant, # = p<0.01, † = p<0.001, error
1062 bars are SD.
1063
1064 **Figure supplement 3: Transcription of ETC subunit encoding genes and translation of**
1065 **mitochondrially encoded proteins are unaffected in mtFAS mutants.** A.-C. Quadruplicate
1066 samples from mtFAS mutant cells and controls were grown under proliferative conditions. Total
1067 RNA was isolated, used as input for mRNA library prep, and sequenced. Resulting data were
1068 aligned to the mouse genome and analyzed for differential expression. ETC subunit encoding
1069 transcripts are shown in red vs. all other transcripts (black). C. Cumulative distribution plots
1070 showing no difference in abundance between ETC encoding transcripts vs. all other genes for
1071 the indicated mtFAS mutant vs. GFP control, p > 0.05, Wilcoxon rank-sum test. D. HEK293T

1072 cells were transiently transfected with human NDUFAB1-Flag or empty vector control along with
1073 the indicated LYRM-V5 constructs, grown for 48 hours after transfection, harvested, and crude
1074 mitochondrial lysates were prepared by differential centrifugation. Flag immunoprecipitation was
1075 performed and eluates were blotted with the indicated antibodies alongside 10% of input. E.-H.
1076 Duplicate samples from the indicated cell lines were grown under proliferative conditions and
1077 subjected to TMT labeling and quantitative proteomics analysis. Relative abundance of the
1078 indicated LYR protein (E.), LYR target (F.), mitochondrially encoded proteins (G.), and MALSU1
1079 (H.). * = $p<0.05$, # = $p<0.01$, error bars are SD. All statistical comparisons shown are between
1080 mtFAS mutants and GFP-1 clone.
1081
1082 **Figure supplement 4: Impairment of mtFAS causes changes in purine abundance and**
1083 **TCA cycle flux.** A.–E. Triplicate biological samples from mtFAS mutant cell lines or GFP control
1084 were grown under standard proliferative conditions in high glucose media (25mM) and
1085 harvested for steady-state metabolomics analysis by LC-MS. Shown are relative pool sizes for
1086 the indicated metabolites. * = $p<0.05$, # = $p<0.01$, error bars are SD. F.-N. Triplicate biological
1087 samples of the indicated genotype were labeled with $U^{13}C$glutamine for 5 minutes, 15 minutes,
1088 30 minutes, or 1 hour, harvested, and analyzed via GC-MS for the indicated metabolite
1089 isotopologues. * = $p<0.05$, # = $p<0.01$, † = $p<0.001$, ‡ = $p<0.0001$, error bars are SD. Symbols
1090 indicate statistical comparison to GFP control in the order *Mcat*, *Oxsm*, *Mecr*.
1091
1092 **Figure supplement 5: Skeletal myoblast differentiation is delayed in mtFAS mutant cell**
1093 **lines.** A. Cells of the indicated genotypes were plated and grown for 24 hours under proliferative
1094 conditions (day -1), then switched to 2% horse serum differentiation medium at 95% confluency
1095 (day 0). Medium was replaced daily for the indicated number of days. Plates were imaged at the
1096 indicated time points. B.-C. Quadruplicate samples from mtFAS mutant cells and controls were
1097 plated and allowed to adhere overnight, then harvested at Day -1 (proliferative, ~70%

1098 confluency), Day 0 (~95% confluent), or Day 1 after switching to 2% horse serum differentiation
1099 medium for 24 hours. Total RNA was isolated, used as input for mRNA library prep, and
1100 sequenced. Resulting data were aligned to the mouse genome and analyzed for differential
1101 expression. Transcripts for differentiation related proteins from panel (A) are shown in purple vs.
1102 all other transcripts (gray). B. Oxsm mutant vs. GFP controls after 24 hours in differentiating
1103 media. C. Cumulative distribution plots of differentiation related transcripts vs. all other genes for
1104 the indicated genotypes, $p > 0.05$, Wilcoxon rank-sum test. D. Change in expression of
1105 transcripts from Day -1 to Day 0 for mtFAS mutant cell lines and GFP controls.
1106
1107 **Supplemental Table Legends**
1108
1109 **Supplemental Table 1:** All steady-state metabolites measured via LCMS. Values shown are
1110 average fold change from mean GFP abundance.
1111
1112 **Supplemental Table 2**: Relative expression of proteins associated with skeletal muscle
1113 differentiation from SL-TMT experiment. Values are arbitrary units.
1114
1115 **Resource Availability**
1116
1117 All unique/stable reagents generated within this study are available from the corresponding
1118 author, Jared Rutter, (rutter@biochem.utah.edu) upon request without restriction.
1119
1120 ***Data and Code Availability***
1121 The quantitative proteomics data RAW files will be made available upon request, in addition that
1122 data have been deposited to the ProteomeXchange Consortium via the PRIDE (Perez-Riverol

1123 et al., 2019) partner repository with the dataset identifier {pending}. The code used to process

1124 these data is available at Github https://github.com/j-berg/nowinski_2020.

1125 Sequencing data have been deposited at the Gene Expression Omnibus

1126 (http://www.ncbi.nlm.nih.gov/geo) under accession number GSE148617, and will be made

1127 publicly available before publication.

1128

1129 **Supplemental Table 1:**

1130

Metabolite	GFP-1	Mcat-1	Oxsm-1	Mecr-1
OXOGLUTARATE	1.000	14.342	22.874	16.937
GLUTATHIONE REDUCED	1.000	2.590	9.888	5.128
OXIDIZED GLUTATHIONE	1.000	3.229	7.622	4.521
2-HYDROXYGLUTARIC	1.000	4.121	4.670	2.290
INOSINE	1.000	0.797	3.535	0.521
HYPOXANTHINE	1.000	1.303	3.394	0.771
DEOXYGUANOSINE-MONOPHOSPHATE	1.000	1.437	3.118	1.101
BETAINE ALDEHYDE	1.000	2.179	3.085	3.982
6-HYDROXYDOPAMINE	1.000	2.085	3.051	3.791
N-METHYLGLUTAMATE	1.000	2.995	2.845	3.340
OXOADIPATE	1.000	3.345	2.832	2.380
NICOTINAMIDE MONONUCLEOTIDE	1.000	0.981	2.782	1.168
AMINOADIPATE	1.000	2.086	2.649	2.014
PYRUVATE	1.000	2.641	2.318	3.455
GUANOSINE MONOPHOSPHATE	1.000	0.954	2.102	0.860

CYSTEINE	1.000	1.032	1.949	1.620
2-KETOHEXANOIC	1.000	2.995	1.822	1.308
Fructose 1,6-bisphosphate	1.000	0.911	1.818	2.217
URATE-2	1.000	4.273	1.817	1.944
URATE-1	1.000	4.273	1.816	1.944
ADENOSINE-MONOPHOSPHATE	1.000	0.979	1.804	0.632
DIETHANOLAMINE	1.000	1.141	1.725	1.052
3-METHYL-2-OXOVALERATE	1.000	2.918	1.686	1.125
DL-2-AMINOCTANOATE	1.000	0.876	1.662	1.456
KETOLEUCINE	1.000	2.873	1.655	1.110
KYNURENINE	1.000	1.979	1.650	1.300
4-GUANIDINOBUTANOATE-2	1.000	1.682	1.567	1.231
TRIMETHYLAMINE	1.000	1.844	1.538	1.408
URIDINE MONOPHOSPHATE	1.000	1.313	1.536	1.289
AICAR	1.000	0.721	1.532	1.190
N,N-DIMETHYLARGININE	1.000	1.967	1.532	1.621
Octanoate	1.000	1.231	1.496	1.498
LPC(18:1)	1.000	2.071	1.458	1.226
CYTIDINE MONOPHOSPHATE	1.000	1.318	1.449	0.670
4-HYDROXY-3-METHOXYPHENYLGLYCOL	1.000	1.450	1.446	1.798
SPERMIDINE	1.000	1.247	1.446	1.169
3-Hydroxysebacic acid	1.000	1.244	1.425	1.369
OXOPROLINE	1.000	2.313	1.402	1.466
hexanoylcarnitine	1.000	1.220	1.395	1.842

MANDELATE	1.000	0.865	1.390	1.545
2-HYDROXYPHENYLACETATE	1.000	1.067	1.377	1.545
CYTIDINE	1.000	3.482	1.341	1.308
PALMITATE	1.000	0.968	1.336	1.284
LPC(16:0)	1.000	2.650	1.317	1.425
6-Phosphonoglucono-D-lactone	1.000	0.645	1.302	2.068
HYDROXYISOCAPROIC	1.000	1.292	1.298	1.497
MANNOSE 6-PHOSPHATE	1.000	0.527	1.298	1.507
ACETOIN	1.000	1.245	1.288	1.221
GLUCOSE 6-PHOSPHATE	1.000	0.543	1.274	1.515
GLUCOSE 1-PHOSPHATE	1.000	0.541	1.273	1.513
FRUCTOSE 6-PHOSPHATE	1.000	0.541	1.273	1.513
D-RIBOSE 5-PHOSPHATE	1.000	0.786	1.268	1.366
GLUTARATE	1.000	1.238	1.263	1.323
DEOXYCYTIDINE-DIPHOSPHATE	1.000	0.531	1.259	0.297
SEDOHEPTULOSE-7-PHOSPHATE	1.000	0.439	1.244	1.333
BETA-GLYCEROPHOSPHATE	1.000	1.207	1.231	1.082
RIBULOSE-5-PHOSPHATE	1.000	0.754	1.229	1.325
URIDINE 5'-DIPHOSPHATE	1.000	1.344	1.229	1.316
Ribose-5-phosphate	1.000	0.756	1.227	1.326
Xylulose-5-phosphate	1.000	0.751	1.225	1.323
7-HYDROXYOCTANOATE	1.000	1.124	1.224	1.242
SPERMINE	1.000	0.521	1.222	1.276
undecanedioic acid	1.000	1.140	1.219	1.273
GLYCEROL 3-PHOSPHATE	1.000	1.194	1.218	1.052

LEUCINE	1.000	0.958	1.217	0.915
METHYL 4-AMINOBUTYRATE	1.000	1.828	1.215	1.137
O-SUCCINYL-HOMOSERINE-2	1.000	0.993	1.200	1.410
SUBERATE	1.000	1.093	1.194	1.226
Dimethyl adipate	1.000	1.092	1.193	1.213
PROPIONYLCHOLINE	1.000	1.185	1.190	1.270
2-ETHYLOCTANEDIOATE	1.000	1.139	1.190	1.254
SEBACATE	1.000	1.139	1.190	1.254
DEOXYCYTIDINE MONOPHOSPHATE-1	1.000	1.017	1.188	1.255
DEOXYINOSINE	1.000	0.988	1.186	1.095
6-CARBOXYHEXANOATE	1.000	1.116	1.169	1.241
L-CARNITINE	1.000	1.049	1.163	1.526
Azelaic acid	1.000	1.173	1.161	1.209
Butyrylcarnitine	1.000	1.180	1.161	1.536
CREATINE	1.000	1.012	1.158	1.099
GLYCOLATE	1.000	0.625	1.152	2.708
4-HYDROXYBENZOATE	1.000	1.049	1.143	0.998
LACTATE	1.000	1.412	1.142	1.397
AZELATE	1.000	1.145	1.142	1.179
THYMIDINE	1.000	1.258	1.141	1.086
SALICYLATE	1.000	1.020	1.136	1.235
MONOMETHYLGLUTARATE	1.000	1.171	1.135	1.184
NICOTINAMIDE-1	1.000	1.777	1.124	1.248
GLYCERALDEHYDE	1.000	1.405	1.123	1.376
P-HYDROXYPHENYLACETATE	1.000	0.700	1.123	1.140

2-METHYLGLUTARATE	1.000	1.133	1.118	1.176
METHYGLUTARATE	1.000	1.166	1.118	1.181
N-ACETYLNEURAMINATE	1.000	1.755	1.114	0.815
ADIPATE	1.000	1.052	1.113	1.131
LYSINE	1.000	1.734	1.110	1.025
4-HYDROXYPHENYLPYRUVATE	1.000	1.348	1.105	0.792
3-HYDROXYMETHYLGLUTARATE	1.000	1.349	1.099	0.966
DEOXYGUANOSINE	1.000	1.168	1.097	1.162
BUTANOATE	1.000	1.524	1.089	1.083
4-HYDROXYBENZALDEHYDE	1.000	1.347	1.080	0.762
PANTOTHENATE	1.000	2.106	1.078	0.682
THYMIDINE-MONOPHOSPHATE	1.000	0.800	1.072	0.607
NAD+	1.000	1.270	1.068	1.022
octanoylcarnitine	1.000	1.324	1.058	1.234
DEOXYCYTIDINE-1	1.000	1.612	1.056	0.882
PYRAZOLE	1.000	1.213	1.054	0.824
SACCHARATE	1.000	0.844	1.049	0.988
7-HYDROXYOCTANOATE DIMER	1.000	1.068	1.047	1.003
GLYCEROPHOSPHOCHOLINE	1.000	2.345	1.039	0.870
URIDINE	1.000	1.203	1.036	1.257
PYROGLUTAMATE	1.000	2.255	1.034	2.031
HYPOTAURINE	1.000	0.559	1.033	1.901
6-PHOSPHOGLUCONATE	1.000	0.661	1.033	1.166
TAURINE	1.000	0.689	1.031	1.444
N-METHYLASPARTATE	1.000	0.735	1.024	0.995

GLUTAMATE	1.000	0.735	1.024	0.995
MEVALONATE	1.000	1.130	1.017	1.477
SUCCINATE	1.000	2.157	1.016	0.868
2-DEOXY-D-GLUCOSE	1.000	0.947	1.009	0.227
GLUCURONATE	1.000	0.814	1.009	1.236
ITACONATE	1.000	1.129	1.007	1.047
GALACTARATE	1.000	1.157	1.003	1.067
GALACTURONATE	1.000	0.807	1.001	1.212
TYROSINE	1.000	1.548	0.996	0.842
HOMOSERINE	1.000	0.018	0.994	1.280
ALLOTHREONINE	1.000	0.018	0.994	1.281
N-ACETYLASPARAGINE	1.000	1.280	0.986	0.795
3-(3,4,5-Trimethoxyphenyl)propanoic acid	1.000	1.102	0.980	0.860
2-AMINOPHENOL-2	1.000	1.427	0.978	1.034
XANTHOSINE	1.000	1.247	0.977	0.902
PHENYLETHANOLAMINE	1.000	1.041	0.976	1.019
PYRIDOXINE-2	1.000	1.533	0.976	1.121
PYRIDOXINE-1	1.000	1.533	0.975	1.121
Dodecanoic acid	1.000	0.938	0.971	1.211
L-ORNITHINE	1.000	1.148	0.966	0.963
4-ACETAMIDOBUTANOATE	1.000	1.766	0.965	1.040
URACIL-1	1.000	1.194	0.964	0.922
4-PYRIDOXATE	1.000	2.121	0.961	1.134
2-METHYLMALEATE	1.000	0.978	0.949	0.897

TRYPTOPHAN	1.000	1.589	0.942	0.778
THREONINE	1.000	0.790	0.941	0.899
BETAINE	1.000	1.086	0.940	0.795
METHYLTHIOADENOSINE	1.000	1.120	0.936	0.889
GLYCOCHOLATE	1.000	1.915	0.932	0.935
N,N,N-TRIMETHYLLYSINE	1.000	0.985	0.927	1.009
D-ORNITHINE	1.000	1.230	0.924	0.946
UREA	1.000	0.994	0.922	1.288
METHIONINE-1	1.000	1.381	0.921	0.819
GLYCERATE	1.000	1.286	0.919	1.053
DIHYDROXYACETONEPHOSPHATE	1.000	0.493	0.913	0.629
Glyceraldehyde 3-phosphate	1.000	0.499	0.909	0.640
3-(2-HYDROXYPHENYL)PROPANOATE	1.000	0.978	0.908	1.544
ERYTHROSE-4-PHOSPHATE	1.000	0.589	0.907	1.292
TRIGONELLINE	1.000	0.943	0.906	0.945
Isovalerylcarnitine	1.000	1.468	0.901	1.140
PIPECOLATE	1.000	1.069	0.900	0.750
PHENYLALANINE	1.000	1.437	0.894	0.789
NICOTINATE-1	1.000	1.052	0.884	0.793
NICOTINAMIDE-2	1.000	1.403	0.884	0.907
ARGININE	1.000	1.136	0.882	0.918
HIPPURATE	1.000	1.941	0.880	0.895
METHIONINE SULFOXIDE	1.000	0.653	0.867	0.822
CREATININE	1.000	1.123	0.858	0.709
XANTHINE-2	1.000	1.683	0.856	0.814

O-ACETYLSERINE	1.000	0.761	0.849	0.789
PHENYLLACTATE	1.000	0.996	0.847	1.394
5-HYDROXYTRYPTOPHAN	1.000	1.707	0.845	0.695
PHOSPHOCREATINE	1.000	0.750	0.843	0.801
1-AMINOCYCLOPROPANECARBOXYLATE	1.000	0.880	0.838	0.883
RHAMNOSE	1.000	1.118	0.833	0.682
ISOLEUCINE	1.000	1.278	0.832	0.939
FOLATE	1.000	1.768	0.831	0.949
RAFFINOSE	1.000	1.188	0.829	0.923
DEOXYCARNITINE	1.000	0.739	0.814	1.076
HISTIDINE	1.000	0.931	0.812	0.836
METHIONINE-2	1.000	1.447	0.801	0.668
STACHYOSE	1.000	1.179	0.797	0.840
ASPARAGINE	1.000	0.456	0.796	0.677
ALLANTOIN	1.000	1.511	0.796	0.830
GLYCOCHENODEOXYCHOLATE	1.000	1.834	0.794	0.919
RIBOFLAVIN	1.000	1.917	0.792	0.893
BENZYLAMINE	1.000	1.147	0.791	0.814
URACIL-2	1.000	1.137	0.790	0.786
S-ADENOSYLMETHIONINE	1.000	1.087	0.786	0.450
2-HYDROXY-4-(METHYLTHIO)BUTANOATE	1.000	0.704	0.783	1.854
N-ALPHA-ACETYLLYSINE	1.000	1.166	0.782	0.627
N-ACETYLMETHIONINE	1.000	0.685	0.779	1.088

GLUCONATE	1.000	0.413	0.757	1.413
VALINE	1.000	1.152	0.741	0.787
4-GUANIDINOBUTANOATE	1.000	1.041	0.740	0.741
N-ACETYLASPARTATE	1.000	0.883	0.740	0.709
GLYCINE	1.000	0.806	0.739	0.839
GALACTITOL	1.000	0.882	0.730	1.035
MANNITOL	1.000	0.882	0.730	1.035
GLYOXYLATE	1.000	0.838	0.720	1.067
2-HYDROXYBUTYRATE	1.000	0.941	0.712	0.602
GLUTAMINE	1.000	0.859	0.697	0.584
HYDROXYPHENYLLACTATE	1.000	0.826	0.689	1.462
1-METHYL-L-HISTIDINE	1.000	1.061	0.688	0.376
3,4-Dihydroxyhydrocinnamic acid	1.000	0.824	0.686	1.451
Hydroxyphenyllactic acid	1.000	0.827	0.665	1.496
KYNURENATE	1.000	1.048	0.653	0.731
N-ACETYLALANINE	1.000	0.623	0.649	1.515
CARNOSINE	1.000	0.872	0.638	1.402
GLUTARYLCARNITINE	1.000	2.196	0.637	0.776
N-ACETYLGLYCINE	1.000	0.768	0.624	0.612
PROPIONYLCARNITINE	1.000	1.413	0.623	0.705
2-HYDROXYPYRIDINE	1.000	1.007	0.621	0.595
CITRULLINE	1.000	0.745	0.617	0.843
HEXOSE	1.000	0.815	0.617	1.475
GLUCOSAMINE 6-PHOSPHATE	1.000	0.325	0.614	1.020
ETHYLMALONATE	1.000	1.232	0.571	0.688

URIDINE DIPHOSPHATE GLUCOSE	1.000	1.098	0.562	0.749
CITRAMALATE	1.000	1.048	0.562	0.509
UDPgalactose	1.000	1.128	0.553	0.772
SALSOLINOL-2	1.000	1.541	0.547	0.747
N-ACETYLLEUCINE	1.000	1.059	0.536	0.625
O-PHOSPHOETHANOLAMINE	1.000	0.309	0.533	0.624
ETHANOLAMINE PHOSPHATE	1.000	0.310	0.532	0.627
BETA-ALANINE	1.000	0.399	0.519	0.794
SERINE	1.000	0.516	0.497	0.600
SARCOSINE	1.000	0.402	0.492	0.771
URIDINE DIPHOSPHATE-N-ACETYLGLUCOSAMINE	1.000	1.069	0.484	0.836
URIDINE DIPHOSPHATE-N-ACETYLGALACTOSAMINE	1.000	1.078	0.474	0.844
ANSERINE	1.000	0.950	0.459	0.873
N-FORMYL-L-METHIONINE	1.000	0.327	0.448	1.210
SALSOLINOL-1	1.000	1.082	0.420	0.762
cis-ACONITATE-1	1.000	0.727	0.399	0.498
PHOSPHOSERINE	1.000	0.473	0.396	0.670
N-ACETYLPUTRESCINE	1.000	0.360	0.384	0.342
PHENYLACETATE	1.000	0.883	0.383	1.421
N-ACETYLPHENYLALANINE	1.000	1.005	0.382	0.487
FUMARATE	1.000	0.490	0.379	0.935
MALEATE	1.000	0.489	0.369	0.905
SORBITOL	1.000	0.540	0.366	1.144

MALATE	1.000	0.412	0.336	0.898
O-ACETYLCARNITINE-2	1.000	0.685	0.315	0.275
L-ALANINE	1.000	0.299	0.311	0.443
D-ALANINE	1.000	0.294	0.309	0.438
OPHTHALMATE-2	1.000	0.670	0.301	0.448
DIMETHYLGLYCINE	1.000	0.730	0.300	1.356
CITRATE	1.000	0.712	0.300	0.449
PROLINE	1.000	0.802	0.281	0.588
GAMMA-AMINOBUTYRATE	1.000	0.185	0.241	1.302
PORPHOBILINOGEN-1	1.000	1.162	0.214	0.949
O-ACETYLCARNITINE	1.000	0.388	0.213	0.266
PHOSPHORYLCHOLINE	1.000	0.093	0.196	0.338
GUANIDINOACETATE	1.000	0.165	0.176	0.070
ASPARTATE	1.000	0.128	0.139	0.235
CYSTINE	1.000	0.663	0.005	0.005

Supplemental Table 2:

Gene Symbol	**Description**	**GFP-1**	**GFP-2**	**Oxsm-1**	**Mecr-1**	**Mecr-2**
Cdh15	CAD15_MOUSE Cadherin-15	14.80	12.63	5.22	8.53	5.35
Myod1	MYOD1_MOUSE Myoblast determination protein 1	12.88	10.20	5.15	9.85	7.56
Tnnt3	TNNT3_MOUSE Troponin T, fast skeletal muscle	23.46	11.06	3.71	6.21	3.24

Tnni2	TNNI2_MOUSE Troponin I, fast skeletal muscle	26.59	9.76	2.73	6.25	2.42
Tnnt2	TNNT2_MOUSE Troponin T, cardiac muscle	29.13	8.47	2.11	6.04	2.08
Tnni1	TNNI1_MOUSE Troponin I, slow skeletal muscle	29.93	10.61	1.46	4.71	1.33
Tnnc1	TNNC1_MOUSE Troponin C, slow skeletal and cardiac muscles	32.32	11.36	0.78	3.76	0.77
Myh1	MYH1_MOUSE Myosin-1	29.34	13.57	2.80	2.02	1.56
Mb	MYG_MOUSE Myoglobin	32.32	11.36	1.44	2.31	1.41
Chdh	CHDH_MOUSE Choline dehydrogenase, mitochondrial	19.97	25.70	1.09	1.60	1.28
Cd44	CD44_MOUSE CD44 antigen	17.76	13.15	4.69	5.60	6.53
Mylpf	MLRS_MOUSE Myosin regulatory light chain 2, skeletal muscle isoform	33.08	9.48	2.23	2.60	1.62
Myh3	MYH3_MOUSE Myosin-3	33.53	9.34	2.91	2.11	1.30
Acta1	ACTS_MOUSE Actin, alpha skeletal muscle	29.41	11.38	1.84	3.74	2.61
Myl1	MYL1_MOUSE Myosin light chain 1/3, skeletal muscle isoform	29.19	12.41	2.05	3.13	1.92
Myl4	MYL4_MOUSE Myosin light chain 4	21.07	8.25	8.05	4.75	5.17

Myl6b	MYL6B_MOUSE Myosin light chain 6B	28.33	7.25	2.69	5.25	4.18
Sorbs2	SRBS2_MOUSE Isoform 2 of Sorbin and SH3 domain-containing protein 2	30.69	13.23	2.43	1.57	1.34
Csrp3	CSRP3_MOUSE Cysteine and glycine-rich protein 3	32.20	11.30	1.17	3.02	1.01
Nrap	NRAP_MOUSE Nebulin-related-anchoring protein	25.07	15.64	2.70	3.72	0.45
Klhl41	KLH41_MOUSE Kelch-like protein 41	19.74	12.08	5.16	5.67	4.70
Ccdc141	A2AST1_MOUSE Coiled-coil protein associated with myosin II and DISC1	27.08	13.57	2.55	3.18	1.65
Neb	A2AQA9_MOUSE Protein Neb	25.63	10.39	3.78	4.87	3.42
Bin1	BIN1_MOUSE Myc box-dependent-interacting protein 1	22.25	11.53	5.00	5.80	4.14
Ckm	KCRM_MOUSE Creatine kinase M-type	20.99	13.62	3.52	6.25	3.63
Ckb	KCRB_MOUSE Creatine kinase B-type	23.97	13.29	2.69	3.22	4.93
Ank1	ANK1_MOUSE Isoform Mu7 of Ankyrin-1	19.68	22.43	0.98	4.80	0.80
Trim72	TRI72_MOUSE Tripartite motif-containing protein 72	27.22	10.64	3.59	4.78	2.27

Itga7	ITA7_MOUSE Integrin alpha-7	17.66	13.34	5.37	5.96	4.66
Akap6	E9Q9K8_MOUSE Protein Akap6	19.39	14.68	4.31	5.04	3.17
Dusp27	DUS27_MOUSE Inactive dual specificity phosphatase 27	15.61	14.64	5.26	6.56	3.95

REFERENCES

Angerer, H. (2015). Eukaryotic LYR Proteins Interact with Mitochondrial Protein Complexes. Biology *4*, 133-150.

Angerer, H., Radermacher, M., Mankowska, M., Steger, M., Zwicker, K., Heide, H., Wittig, I., Brandt, U., and Zickermann, V. (2014). The LYR protein subunit NB4M/NDUFA6 of mitochondrial complex I anchors an acyl carrier protein and is essential for catalytic activity. Proceedings of the National Academy of Sciences of the United States of America *111*, 5207-5212.

Angerer, H., Schonborn, S., Gorka, J., Bahr, U., Karas, M., Wittig, I., Heidler, J., Hoffmann, J., Morgner, N., and Zickermann, V. (2017). Acyl modification and binding of mitochondrial ACP to multiprotein complexes. Biochimica et biophysica acta *1864*, 1913-1920.

Asp, P., Blum, R., Vethantham, V., Parisi, F., Micsinai, M., Cheng, J., Bowman, C., Kluger, Y., and Dynlacht, B.D. (2011). Genome-wide remodeling of the epigenetic landscape during myogenic differentiation. Proceedings of the National Academy of Sciences of the United States of America *108*, E149-158.

1152 Autio, K.J., Kastaniotis, A.J., Pospiech, H., Miinalainen, I.J., Schonauer, M.S., Dieckmann, C.L.,
1153 and Hiltunen, J.K. (2008). An ancient genetic link between vertebrate mitochondrial fatty acid
1154 synthesis and RNA processing. FASEB journal : official publication of the Federation of
1155 American Societies for Experimental Biology *22*, 569-578.

1156 Beausoleil, S.A., Villen, J., Gerber, S.A., Rush, J., and Gygi, S.P. (2006). A probability-based
1157 approach for high-throughput protein phosphorylation analysis and site localization. Nature
1158 biotechnology *24*, 1285-1292.

1159 Berg, J.A., Belyeu, J.R., Morgan, J.T., Ouyang, Y., Bott, A.J., Quinlan, A.R., Gertz, J., and
1160 Rutter, J. (2020). XPRESSyourself: Enhancing, standardizing, and automating ribosome
1161 profiling computational analyses yields improved insight into data. PLOS Computational Biology
1162 *16*, e1007625.

1163 Birsoy, K., Wang, T., Chen, W.W., Freinkman, E., Abu-Remaileh, M., and Sabatini, D.M. (2015).
1164 An Essential Role of the Mitochondrial Electron Transport Chain in Cell Proliferation Is to Enable
1165 Aspartate Synthesis. Cell *162*, 540-551.

1166 Boniecki, M.T., Freibert, S.A., Muhlenhoff, U., Lill, R., and Cygler, M. (2017). Structure and
1167 functional dynamics of the mitochondrial Fe/S cluster synthesis complex. Nature
1168 communications *8*, 1287.

1169 Broad, D. (2020). DepMap 20Q1 Public.

1170 Brody, S., Oh, C., Hoja, U., and Schweizer, E. (1997). Mitochondrial acyl carrier protein is
1171 involved in lipoic acid synthesis in Saccharomyces cerevisiae. FEBS letters *408*, 217-220.

1172 Brown, A., Rathore, S., Kimanius, D., Aibara, S., Bai, X.C., Rorbach, J., Amunts, A., and
1173 Ramakrishnan, V. (2017). Structures of the human mitochondrial ribosome in native states of
1174 assembly. Nature structural & molecular biology *24*, 866-869.

1175 Cai, Y., Lin, Y., Xiong, X., Lu, J., Zhou, R., Jin, Y., You, Z., Ye, H., Li, F., and Cheng, N. (2019).
1176 Knockdown expression of MECR, a novel gene of mitochondrial FAS II inhibits growth and
1177 colony-formation, promotes apoptosis of hepatocelluar carcinoma cells. Biosci Trends *13*, 234-
1178 244.

1179 Calvo, S.E., Clauser, K.R., and Mootha, V.K. (2016). MitoCarta2. 0: an updated inventory of
1180 mammalian mitochondrial proteins. Nucleic acids research *44*, D1251-D1257.

1181 Chambers, M.C., Maclean, B., Burke, R., Amodei, D., Ruderman, D.L., Neumann, S., Gatto, L.,
1182 Fischer, B., Pratt, B., Egertson, J.*, et al.* (2012). A cross-platform toolkit for mass spectrometry
1183 and proteomics. Nat Biotechnol *30*, 918-920.

1184 Chen, Z., Kastaniotis, A.J., Miinalainen, I.J., Rajaram, V., Wierenga, R.K., and Hiltunen, J.K.
1185 (2009). 17beta-hydroxysteroid dehydrogenase type 8 and carbonyl reductase type 4 assemble
1186 as a ketoacyl reductase of human mitochondrial FAS. FASEB journal : official publication of the
1187 Federation of American Societies for Experimental Biology *23*, 3682-3691.

1188 Clay, H.B., Parl, A.K., Mitchell, S.L., Singh, L., Bell, L.N., and Murdock, D.G. (2016). Altering the
1189 Mitochondrial Fatty Acid Synthesis (mtFASII) Pathway Modulates Cellular Metabolic States and
1190 Bioactive Lipid Profiles as Revealed by Metabolomic Profiling. PloS one *11*, e0151171.

1191 Cory, S.A., Van Vranken, J.G., Brignole, E.J., Patra, S., Winge, D.R., Drennan, C.L., Rutter, J.,
1192 and Barondeau, D.P. (2017). Structure of human Fe-S assembly subcomplex reveals
1193 unexpected cysteine desulfurase architecture and acyl-ACP-ISD11 interactions. Proceedings of
1194 the National Academy of Sciences of the United States of America *114*, E5325-e5334.

1195 Dibley, M.G., Formosa, L.E., Lyu, B., Reljic, B., McGann, D., Muellner-Wong, L., Kraus, F.,
1196 Sharpe, A.J., Stroud, D.A., and Ryan, M.T. (2020). The Mitochondrial Acyl-carrier Protein
1197 Interaction Network Highlights Important Roles for LYRM Family Members in Complex I and
1198 Mitoribosome Assembly. Molecular & cellular proteomics : MCP *19*, 65-77.

1199 Dobin, A., Davis, C.A., Schlesinger, F., Drenkow, J., Zaleski, C., Jha, S., Batut, P., Chaisson,
1200 M., and Gingeras, T.R. (2013). STAR: ultrafast universal RNA-seq aligner. Bioinformatics *29*,
1201 15-21.

1202 Elias, J.E., and Gygi, S.P. (2007). Target-decoy search strategy for increased confidence in
1203 large-scale protein identifications by mass spectrometry. Nat Methods *4*, 207-214.

1204 Elias, J.E., and Gygi, S.P. (2010). Target-decoy search strategy for mass spectrometry-based
1205 proteomics. Methods Mol Biol *604*, 55-71.

1206 Feng, D., Witkowski, A., and Smith, S. (2009). Down-regulation of mitochondrial acyl carrier
1207 protein in mammalian cells compromises protein lipoylation and respiratory complex I and
1208 results in cell death. The Journal of biological chemistry *284*, 11436-11445.

1209 Fiedorczuk, K., Letts, J.A., Degliesposti, G., Kaszuba, K., Skehel, M., and Sazanov, L.A. (2016).
1210 Atomic structure of the entire mammalian mitochondrial complex I. Nature *538*, 406-410.

1211 Floyd, B.J., Wilkerson, E.M., Veling, M.T., Minogue, C.E., Xia, C., Beebe, E.T., Wrobel, R.L.,
1212 Cho, H., Kremer, L.S., Alston, C.L.*, et al.* (2016). Mitochondrial Protein Interaction Mapping
1213 Identifies Regulators of Respiratory Chain Function. Molecular cell *63*, 621-632.

1214 Fujiwara, K., Okamura-Ikeda, K., and Motokawa, Y. (1991). Lipoylation of H-protein of the
1215 glycine cleavage system. The effect of site-directed mutagenesis of amino acid residues around
1216 the lipoyllysine residue on the lipoate attachment. FEBS letters *293*, 115-118.

1217 Funai, K., Song, H., Yin, L., Lodhi, I.J., Wei, X., Yoshino, J., Coleman, T., and Semenkovich,
1218 C.F. (2013). Muscle lipogenesis balances insulin sensitivity and strength through calcium
1219 signaling. J Clin Invest *123*, 1229-1240.

1220 Gao, T., Qian, S., Shen, S., Zhang, X., Liu, J., Jia, W., Chen, Z., and Ye, J. (2019). Reduction of
1221 mitochondrial 3-oxoacyl-ACP synthase (OXSM) by hyperglycemia is associated with deficiency
1222 of alpha-lipoic acid synthetic pathway in kidney of diabetic mice. Biochemical and biophysical
1223 research communications *512*, 106-111.

1224 Ghezzi, D., Goffrini, P., Uziel, G., Horvath, R., Klopstock, T., Lochmuller, H., D'Adamo, P.,
1225 Gasparini, P., Strom, T.M., Prokisch, H.*, et al.* (2009). SDHAF1, encoding a LYR complex-II
1226 specific assembly factor, is mutated in SDH-defective infantile leukoencephalopathy. Nature
1227 genetics *41*, 654-656.

1228 Gorukmez, O., Gorukmez, O., and Havali, C. (2019). Novel MECR Mutation in Childhood-Onset
1229 Dystonia, Optic Atrophy, and Basal Ganglia Signal Abnormalities. Neuropediatrics *50*, 336-337.

1230 Gygi, J.P., Yu, Q., Navarrete-Perea, J., Rad, R., Gygi, S.P., and Paulo, J.A. (2019). Web-Based
1231 Search Tool for Visualizing Instrument Performance Using the Triple Knockout (TKO) Proteome
1232 Standard. J Proteome Res *18*, 687-693.

1233 Heimer, G., Keratar, J.M., Riley, L.G., Balasubramaniam, S., Eyal, E., Pietikainen, L.P.,
1234 Hiltunen, J.K., Marek-Yagel, D., Hamada, J., Gregory, A.*, et al.* (2016). MECR Mutations Cause
1235 Childhood-Onset Dystonia and Optic Atrophy, a Mitochondrial Fatty Acid Synthesis Disorder.
1236 American journal of human genetics *99*, 1229-1244.

1237 Hou, T., Zhang, R., Jian, C., Ding, W., Wang, Y., Ling, S., Ma, Q., Hu, X., Cheng, H., and Wang,
1238 X. (2019). NDUFAB1 confers cardio-protection by enhancing mitochondrial bioenergetics

1239 through coordination of respiratory complex and supercomplex assembly. Cell research *29*,
1240 754-766.

1241 Hunter, J.D. (2007). Matplotlib: A 2D graphics environment. Computing in science & engineering
1242 *9*, 90-95.

1243 Huttlin, E.L., Jedrychowski, M.P., Elias, J.E., Goswami, T., Rad, R., Beausoleil, S.A., Villen, J.,
1244 Haas, W., Sowa, M.E., and Gygi, S.P. (2010). A tissue-specific atlas of mouse protein
1245 phosphorylation and expression. Cell *143*, 1174-1189.

1246 Huttlin, E.L., Ting, L., Bruckner, R.J., Gebreab, F., Gygi, M.P., Szpyt, J., Tam, S., Zarraga, G.,
1247 Colby, G., Baltier, K.*, et al.* (2015). The BioPlex Network: A Systematic Exploration of the
1248 Human Interactome. Cell *162*, 425-440.

1249 Ji, Z.X., Du, C., Wu, G.S., Li, S.Y., An, G.S., Yang, Y.X., Jia, R., Jia, H.T., and Ni, J.H. (2009).
1250 Synergistic up-regulation of muscle LIM protein expression in C2C12 and NIH3T3 cells by
1251 myogenin and MEF2C. Mol Genet Genomics *281*, 1-10.

1252 Joshi, A.K., Zhang, L., Rangan, V.S., and Smith, S. (2003). Cloning, Expression, and
1253 Characterization of a Human 4′-Phosphopantetheinyl Transferase with Broad Substrate
1254 Specificity. Journal of Biological Chemistry *278*, 33142-33149.

1255 Kastaniotis, A.J., Autio, K.J., Sormunen, R.T., and Hiltunen, J.K. (2004). Htd2p/Yhr067p is a
1256 yeast 3-hydroxyacyl-ACP dehydratase essential for mitochondrial function and morphology.
1257 Molecular microbiology *53*, 1407-1421.

1258 Khutornenko, A.A., Dalina, A.A., Chernyak, B.V., Chumakov, P.M., and Evstafieva, A.G. (2014).
1259 The Role of Dihydroorotate Dehydrogenase in Apoptosis Induction in Response to Inhibition of
1260 the Mitochondrial Respiratory Chain Complex III. Acta Naturae *6*, 69-75.

1261 Khutornenko, A.A., Roudko, V.V., Chernyak, B.V., Vartapetian, A.B., Chumakov, P.M., and
1262 Evstafieva, A.G. (2010). Pyrimidine biosynthesis links mitochondrial respiration to the p53
1263 pathway. Proceedings of the National Academy of Sciences of the United States of America
1264 *107*, 12828-12833.

1265 Kim, D.G., Yoo, J.C., Kim, E., Lee, Y.S., Yarishkin, O.V., Lee, D.Y., Lee, K.H., Hong, S.G.,
1266 Hwang, E.M., and Park, J.Y. (2014). A Novel Cytosolic Isoform of Mitochondrial Trans-2-Enoyl-
1267 CoA Reductase Enhances Peroxisome Proliferator-Activated Receptor alpha Activity.
1268 Endocrinol Metab (Seoul) *29*, 185-194.

1269 Kim, S., Li, Q., Dang, C.V., and Lee, L.A. (2000). Induction of ribosomal genes and hepatocyte
1270 hypertrophy by adenovirus-mediated expression of c-Myc in vivo. Proceedings of the National
1271 Academy of Sciences of the United States of America *97*, 11198-11202.

1272 Kursu, V.A., Pietikainen, L.P., Fontanesi, F., Aaltonen, M.J., Suomi, F., Raghavan Nair, R.,
1273 Schonauer, M.S., Dieckmann, C.L., Barrientos, A., Hiltunen, J.K.*, et al.* (2013). Defects in
1274 mitochondrial fatty acid synthesis result in failure of multiple aspects of mitochondrial biogenesis
1275 in Saccharomyces cerevisiae. Molecular microbiology *90*, 824-840.

1276 Li, H., Yuan, S., Minegishi, Y., Suga, A., Yoshitake, K., Sheng, X., Ye, J., Smith, S., Bunkoczi,
1277 G., Yamamoto, M.*, et al.* (2020). Novel mutations in malonyl-CoA-acyl carrier protein
1278 transacylase provoke autosomal recessive optic neuropathy. Human molecular genetics *29*,
1279 444-458.

1280 Love, M.I., Huber, W., and Anders, S. (2014). Moderated estimation of fold change and
1281 dispersion for RNA-seq data with DESeq2. Genome Biol *15*, 550.

1282 Majmudar, J.D., Feng, X., Fox, N.G., Nabhan, J.F., Towle, T., Ma, T., Gooch, R., Bulawa, C.,
1283 Yue, W.W., and Martelli, A. (2019). 4'-Phosphopantetheine and long acyl chain-dependent

1284 interactions are integral to human mitochondrial acyl carrier protein function. MedChemComm
1285 *10*, 209-220.

1286 Martin, M. (2011). Cutadapt removes adapter sequences from high-throughput sequencing
1287 reads. EMBnet journal *17*, 10-12.

1288 Matyash, V., Liebisch, G., Kurzchalia, T.V., Shevchenko, A., and Schwudke, D. (2008). Lipid
1289 extraction by methyl-tert-butyl ether for high-throughput lipidomics. Journal of lipid research *49*,
1290 1137-1146.

1291 McAlister, G.C., Huttlin, E.L., Haas, W., Ting, L., Jedrychowski, M.P., Rogers, J.C., Kuhn, K.,
1292 Pike, I., Grothe, R.A., Blethrow, J.D.*, et al.* (2012). Increasing the Multiplexing Capacity of TMTs
1293 Using Reporter Ion Isotopologues with Isobaric Masses. Analytical Chemistry *84*, 7469-7478.

1294 Miinalainen, I.J., Chen, Z.-J., Torkko, J.M., Pirilä, P.L., Sormunen, R.T., Bergmann, U., Qin, Y.-
1295 M., and Hiltunen, J.K. (2003). Characterization of 2-Enoyl Thioester Reductase from Mammals:
1296 AN ORTHOLOG OF Ybr026p/Mrf1′p OF THE YEAST MITOCHONDRIAL FATTY ACID
1297 SYNTHESIS TYPE II. Journal of Biological Chemistry *278*, 20154-20161.

1298 Mikolajczyk, S., and Brody, S. (1990). De novo fatty acid synthesis mediated by acyl-carrier
1299 protein in Neurospora crassa mitochondria. European journal of biochemistry *187*, 431-437.

1300 Mullen, A.R., Hu, Z., Shi, X., Jiang, L., Boroughs, L.K., Kovacs, Z., Boriack, R., Rakheja, D.,
1301 Sullivan, L.B., Linehan, W.M.*, et al.* (2014). Oxidation of alpha-ketoglutarate is required for
1302 reductive carboxylation in cancer cells with mitochondrial defects. Cell Rep *7*, 1679-1690.

1303 Mullen, A.R., Wheaton, W.W., Jin, E.S., Chen, P.-H., Sullivan, L.B., Cheng, T., Yang, Y.,
1304 Linehan, W.M., Chandel, N.S., and DeBerardinis, R.J. (2012). Reductive carboxylation supports
1305 growth in tumour cells with defective mitochondria. Nature *481*, 385-388.

1306 Mullen, A.R., Wheaton, W.W., Jin, E.S., Chen, P.H., Sullivan, L.B., Cheng, T., Yang, Y.,
1307 Linehan, W.M., Chandel, N.S., and DeBerardinis, R.J. (2011). Reductive carboxylation supports
1308 growth in tumour cells with defective mitochondria. Nature *481*, 385-388.

1309 Na, U., Yu, W., Cox, J., Bricker, D.K., Brockmann, K., Rutter, J., Thummel, C.S., and Winge,
1310 D.R. (2014). The LYR factors SDHAF1 and SDHAF3 mediate maturation of the iron-sulfur
1311 subunit of succinate dehydrogenase. Cell metabolism *20*, 253-266.

1312 Nair, R.R., Keratar, J.M., Autio, K.J., Masud, A.J., Finnila, M.A.J., Autio-Harmainen, H.I.,
1313 Miinalainen, I.J., Nieminen, P.A., Hiltunen, J.K., and Kastaniotis, A.J. (2017). Genetic
1314 modifications of Mecr reveal a role for mitochondrial 2-enoyl-CoA/ACP reductase in placental
1315 development in mice. Human molecular genetics *26*, 2104-2117.

1316 Nair, R.R., Koivisto, H., Jokivarsi, K., Miinalainen, I.J., Autio, K.J., Manninen, A., Poutiainen, P.,
1317 Tanila, H., Hiltunen, J.K., and Kastaniotis, A.J. (2018). Impaired Mitochondrial Fatty Acid
1318 Synthesis Leads to Neurodegeneration in Mice. The Journal of neuroscience : the official journal
1319 of the Society for Neuroscience *38*, 9781-9800.

1320 Navarrete-Perea, J., Yu, Q., Gygi, S.P., and Paulo, J.A. (2018). Streamlined Tandem Mass Tag
1321 (SL-TMT) Protocol: An Efficient Strategy for Quantitative (Phospho)proteome Profiling Using
1322 Tandem Mass Tag-Synchronous Precursor Selection-MS3. J Proteome Res *17*, 2226-2236.

1323 Ni, M., Solmonson, A., Pan, C., Yang, C., Li, D., Notzon, A., Cai, L., Guevara, G., Zacharias,
1324 L.G., Faubert, B.*, et al.* (2019). Functional Assessment of Lipoyltransferase-1 Deficiency in
1325 Cells, Mice, and Humans. Cell Rep *27*, 1376-1386.e1376.

1326 Nowinski, S.M., Van Vranken, J.G., Dove, K.K., and Rutter, J. (2018). Impact of Mitochondrial
1327 Fatty Acid Synthesis on Mitochondrial Biogenesis. Current biology : CB *28*, R1212-r1219.

1328 Pagliarini, D.J., Calvo, S.E., Chang, B., Sheth, S.A., Vafai, S.B., Ong, S.-E., Walford, G.A.,
1329 Sugiana, C., Boneh, A., and Chen, W.K. (2008). A mitochondrial protein compendium elucidates
1330 complex I disease biology. Cell *134*, 112-123.

1331 Paulo, J.A. (2014). Nicotine alters the proteome of two human pancreatic duct cell lines. JOP :
1332 Journal of the pancreas *15*, 465-474.

1333 Paulo, J.A., and Gygi, S.P. (2015). A comprehensive proteomic and phosphoproteomic analysis
1334 of yeast deletion mutants of 14-3-3 orthologs and associated effects of rapamycin. Proteomics
1335 *15*, 474-486.

1336 Paulo, J.A., and Gygi, S.P. (2017). Nicotine-induced protein expression profiling reveals
1337 mutually altered proteins across four human cell lines. Proteomics *17*.

1338 Paulo, J.A., O'Connell, J.D., and Gygi, S.P. (2016). A Triple Knockout (TKO) Proteomics
1339 Standard for Diagnosing Ion Interference in Isobaric Labeling Experiments. J Am Soc Mass
1340 Spectrom *27*, 1620-1625.

1341 Pavlova, N.N., and Thompson, C.B. (2016). The Emerging Hallmarks of Cancer Metabolism.
1342 Cell metabolism *23*, 27-47.

1343 Perez-Riverol, Y., Csordas, A., Bai, J., Bernal-Llinares, M., Hewapathirana, S., Kundu, D.J.,
1344 Inuganti, A., Griss, J., Mayer, G., Eisenacher, M.*, et al.* (2019). The PRIDE database and
1345 related tools and resources in 2019: improving support for quantification data. Nucleic Acids
1346 Res *47*, D442-D450.

1347 Rathore, A., Chu, Q., Tan, D., Martinez, T.F., Donaldson, C.J., Diedrich, J.K., Yates, J.R., 3rd,
1348 and Saghatelian, A. (2018). MIEF1 Microprotein Regulates Mitochondrial Translation.
1349 Biochemistry *57*, 5564-5575.

1350 Rockwood, A.L., and Haimi, P. (2006). Efficient calculation of accurate masses of isotopic
1351 peaks. J Am Soc Mass Spectrom *17*, 415-419.

1352 Rogerson, P.J., Jamali, M., and Skerjanc, I.S. (2002). The C-terminus of myogenin, but not
1353 MyoD, targets upregulation of MEF2C expression. FEBS letters *524*, 134-138.

1354 Runswick, M.J., Fearnley, I.M., Skehel, J.M., and Walker, J.E. (1991). Presence of an acyl
1355 carrier protein in NADH:ubiquinone oxidoreductase from bovine heart mitochondria. FEBS
1356 letters *286*, 121-124.

1357 Sanchez, E., Lobo, T., Fox, J.L., Zeviani, M., Winge, D.R., and Fernandez-Vizarra, E. (2013).
1358 LYRM7/MZM1L is a UQCRFS1 chaperone involved in the last steps of mitochondrial Complex
1359 III assembly in human cells. Biochimica et biophysica acta *1827*, 285-293.

1360 Schneider, R., Brors, B., Massow, M., and Weiss, H. (1997). Mitochondrial fatty acid synthesis:
1361 a relic of endosymbiontic origin and a specialized means for respiration. FEBS letters *407*, 249-
1362 252.

1363 Schneider, R., Massow, M., Lisowsky, T., and Weiss, H. (1995). Different respiratory-defective
1364 phenotypes of Neurospora crassa and Saccharomyces cerevisiae after inactivation of the gene
1365 encoding the mitochondrial acyl carrier protein. Current genetics *29*, 10-17.

1366 Smith, S. (1994). The animal fatty acid synthase: one gene, one polypeptide, seven enzymes.
1367 FASEB journal : official publication of the Federation of American Societies for Experimental
1368 Biology *8*, 1248-1259.

1369 Smith, S., Witkowski, A., Moghul, A., Yoshinaga, Y., Nefedov, M., de Jong, P., Feng, D., Fong,
1370 L., Tu, Y., Hu, Y.*, et al.* (2012). Compromised mitochondrial fatty acid synthesis in transgenic
1371 mice results in defective protein lipoylation and energy disequilibrium. PloS one *7*, e47196.

1372 Solmonson, A., and DeBerardinis, R.J. (2018). Lipoic acid metabolism and mitochondrial redox
1373 regulation. The Journal of biological chemistry *293*, 7522-7530.

1374 Soloveychik, M., Xu, M., Zaslaver, O., Lee, K., Narula, A., Jiang, R., Rosebrock, A.P., Caudy,
1375 A.A., and Meneghini, M.D. (2016). Mitochondrial control through nutritionally regulated global
1376 histone H3 lysine-4 demethylation. Sci Rep *6*, 37942.

1377 Spinazzi, M., Casarin, A., Pertegato, V., Salviati, L., and Angelini, C. (2012). Assessment of
1378 mitochondrial respiratory chain enzymatic activities on tissues and cultured cells. Nat Protoc *7*,
1379 1235-1246.

1380 Sullivan, L.B., Gui, D.Y., Hosios, A.M., Bush, L.N., Freinkman, E., and Vander Heiden, M.G.
1381 (2015). Supporting Aspartate Biosynthesis Is an Essential Function of Respiration in
1382 Proliferating Cells. Cell *162*, 552-563.

1383 Triepels, R., Smeitink, J., Loeffen, J., Smeets, R., Buskens, C., Trijbels, F., and van den Heuvel,
1384 L. (1999). The human nuclear-encoded acyl carrier subunit (NDUFAB1) of the mitochondrial
1385 complex I in human pathology. Journal of inherited metabolic disease *22*, 163-173.

1386 Van Vranken, J.G., Jeong, M.Y., Wei, P., Chen, Y.C., Gygi, S.P., Winge, D.R., and Rutter, J.
1387 (2016). The mitochondrial acyl carrier protein (ACP) coordinates mitochondrial fatty acid
1388 synthesis with iron sulfur cluster biogenesis. eLife *5*.

1389 Van Vranken, J.G., Nowinski, S.M., Clowers, K.J., Jeong, M.Y., Ouyang, Y., Berg, J.A., Gygi,
1390 J.P., Gygi, S.P., Winge, D.R., and Rutter, J. (2018). ACP Acylation Is an Acetyl-CoA-Dependent
1391 Modification Required for Electron Transport Chain Assembly. Molecular cell *71*, 567-580.e564.

1392 Wada, H., Shintani, D., and Ohlrogge, J. (1997). Why do mitochondria synthesize fatty acids?
1393 Evidence for involvement in lipoic acid production. Proceedings of the National Academy of
1394 Sciences of the United States of America *94*, 1591-1596.

1395 Waskom, M., Botvinnik, O, O'Kane, D, Hobson, P, Ostblom, J, Lukauskas, S, Gemperline, DC,
1396 Augspurger, T, Halchenko, Y, Cole, JB, Warmenhoven, J, de Ruiter, J, Pye, C, Hoyer, S,
1397 Vanderplas, J, Villalba, S, Kunter, G, Quintero, E, Bachant, P, Martin, M, Meyer, K, Miles, A,
1398 Ram, Y, Brunner, T, Yarkoni, T, Williams, ML, Evans, C, Fitzgerald, C, Brian, Qalieh, A (2018).
1399 mwaskom/seaborn: v0.9.0 (July 2018) doi:10.5281/zenodo.1313201.

1400 Witkowski, A., Joshi, A.K., and Smith, S. (2007). Coupling of the de novo fatty acid biosynthesis
1401 and lipoylation pathways in mammalian mitochondria. The Journal of biological chemistry *282*,
1402 14178-14185.

1403 Yi, X., and Maeda, N. (2005). Endogenous production of lipoic acid is essential for mouse
1404 development. Molecular and cellular biology *25*, 8387-8392.

1405 Zammit, P.S. (2017). Function of the myogenic regulatory factors Myf5, MyoD, Myogenin and
1406 MRF4 in skeletal muscle, satellite cells and regenerative myogenesis. Semin Cell Dev Biol *72*,
1407 19-32.

1408 Zhang, L., Joshi, A.K., Hofmann, J., Schweizer, E., and Smith, S. (2005). Cloning, expression,
1409 and characterization of the human mitochondrial beta-ketoacyl synthase. Complementation of
1410 the yeast CEM1 knock-out strain. The Journal of biological chemistry *280*, 12422-12429.

1411 Zhang, L., Joshi, A.K., and Smith, S. (2003). Cloning, Expression, Characterization, and
1412 Interaction of Two Components of a Human Mitochondrial Fatty Acid Synthase:
1413 MALONYLTRANSFERASE AND ACYL CARRIER PROTEIN. Journal of Biological Chemistry
1414 *278*, 40067-40074.

1415 Zhang, R., Hou, T., Cheng, H., and Wang, X. (2019). NDUFAB1 protects against obesity and
1416 insulin resistance by enhancing mitochondrial metabolism. FASEB journal : official publication of
1417 the Federation of American Societies for Experimental Biology, fj201901117RR.

1418 Zhu, J., Vinothkumar, K.R., and Hirst, J. (2016). Structure of mammalian respiratory complex I.
1419 Nature *536*, 354-358.

1420

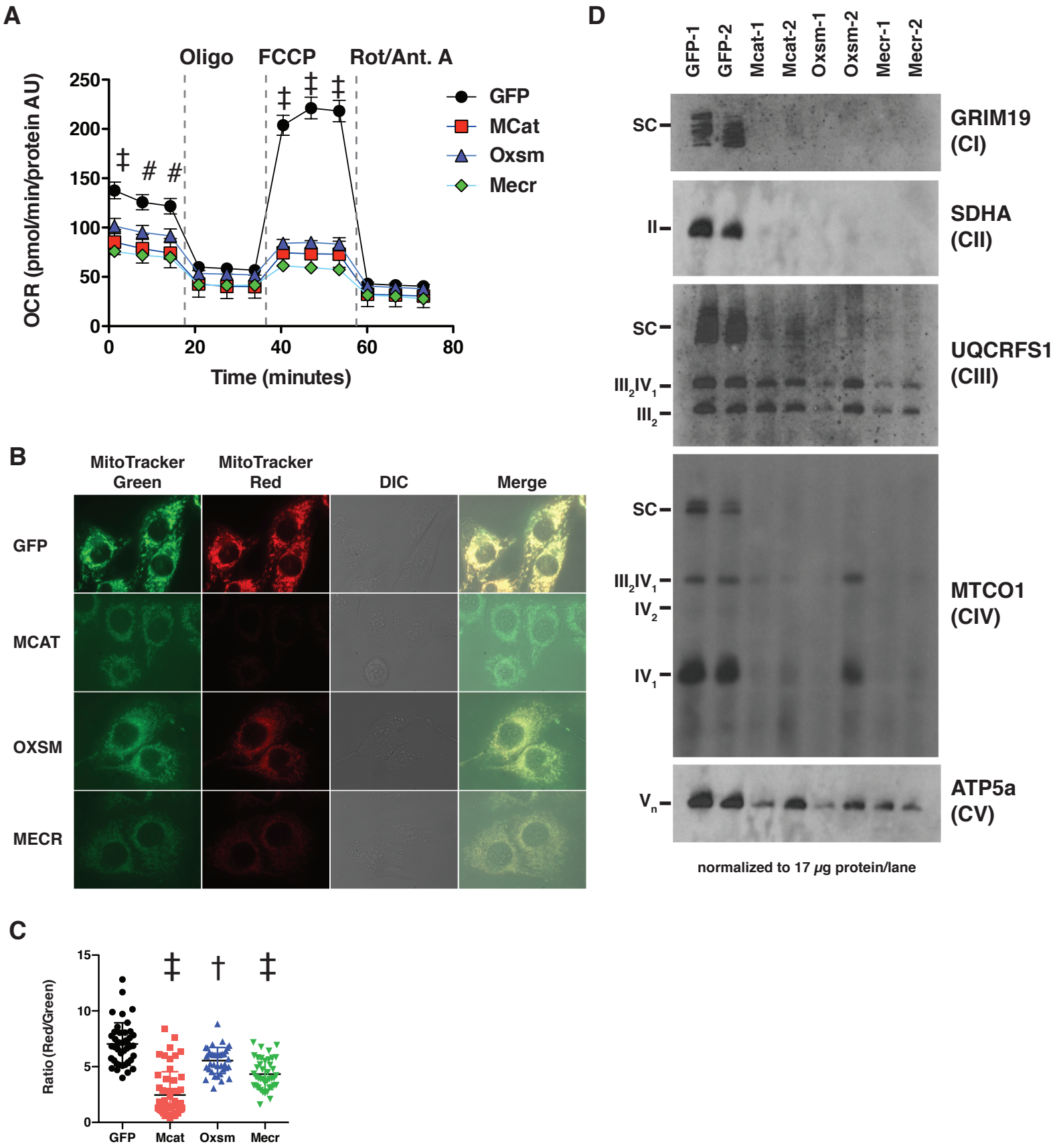
A
Oligo
FCCP
Rot/Ant. A
OCR (pmol/min/protein AU)
Time (minutes)
GFP
MCat
Oxsm
Mecr
B
MitoTracker Green
MitoTracker Red
DIC
Merge
GFP
MCAT
OXSM
MECR
C
Ratio (Red/Green)
GFP
Mcat
Oxsm
Mecr
D
GFP-1
GFP-2
Mcat-1
Mcat-2
Oxsm-1
Oxsm-2
Mecr-1
Mecr-2
GRIM19 (CI)
SDHA (CII)
UQCRFS1 (CIII)
MTCO1 (CIV)
ATP5a (CV)
SC
normalized to 17 μg protein/lane

Figure 2

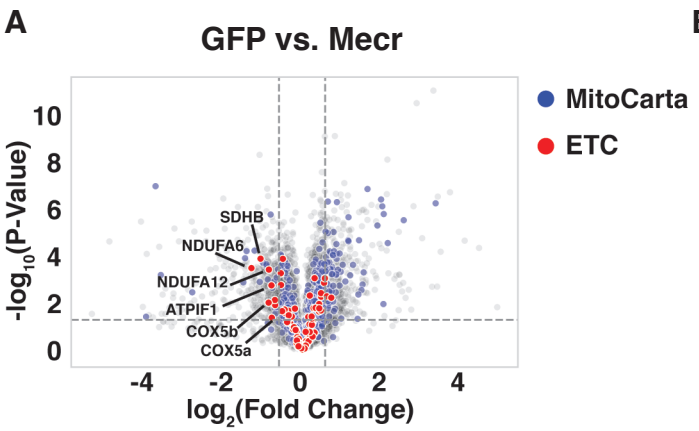
A
GFP vs. Mecr
MitoCarta
ETC
SDHB
NDUFA6
NDUFA12
ATPIF1
COX5b
COX5a
-log10(P-Value)
log2(Fold Change)

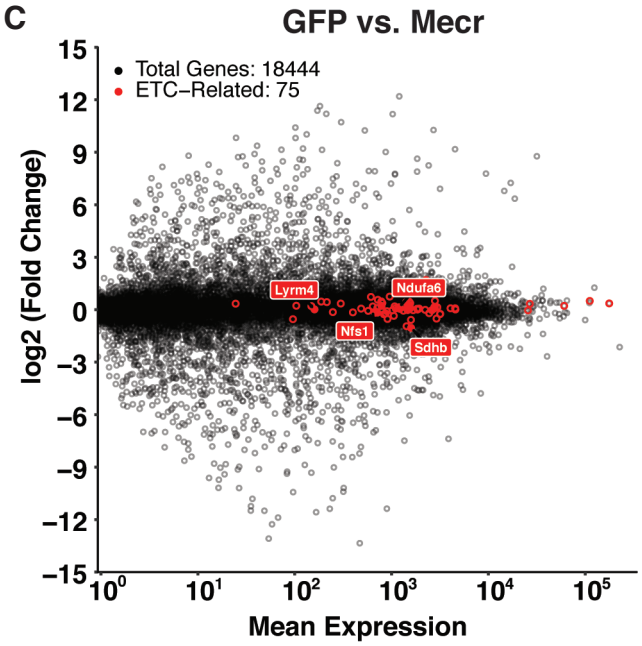
C
GFP vs. Mecr
Total Genes: 18444
ETC–Related: 75
Lyrm4
Ndufa6
Nfs1
Sdhb
log2 (Fold Change)
Mean Expression

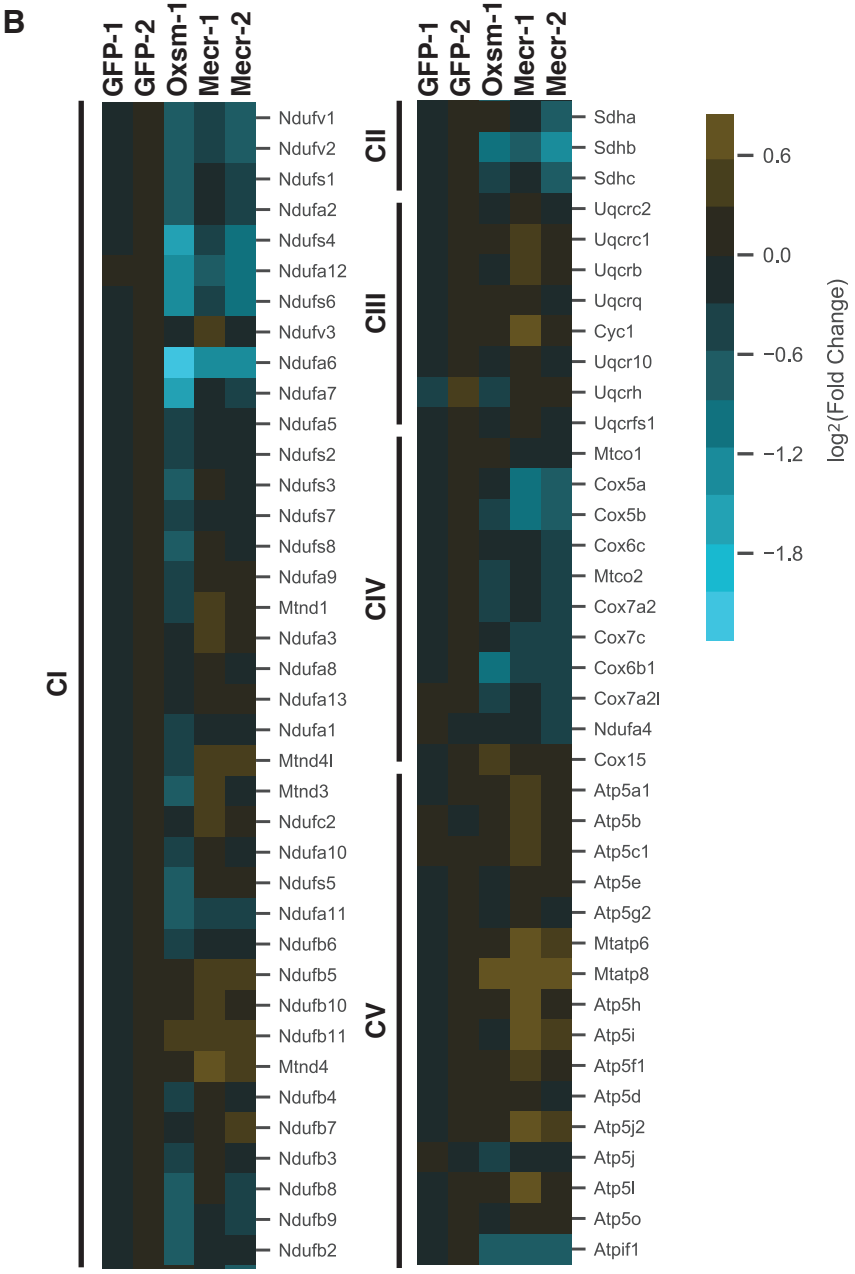
B
GFP-1
GFP-2
Oxsm-1
Mecr-1
Mecr-2
CI
CII
CIII
CIV
CV
Ndufv1
Ndufv2
Ndufs1
Ndufa2
Ndufs4
Ndufa12
Ndufs6
Ndufv3
Ndufa6
Ndufa7
Ndufa5
Ndufs2
Ndufs3
Ndufs7
Ndufs8
Ndufa9
Mtnd1
Ndufa3
Ndufa8
Ndufa13
Ndufa1
Mtnd4l
Mtnd3
Ndufc2
Ndufa10
Ndufs5
Ndufa11
Ndufb6
Ndufb5
Ndufb10
Ndufb11
Mtnd4
Ndufb4
Ndufb7
Ndufb3
Ndufb8
Ndufb9
Ndufb2
Sdha
Sdhb
Sdhc
Uqcrc2
Uqcrc1
Uqcrb
Uqcrq
Cyc1
Uqcr10
Uqcrh
Uqcrfs1
Mtco1
Cox5a
Cox5b
Cox6c
Mtco2
Cox7a2
Cox7c
Cox6b1
Cox7a2l
Ndufa4
Cox15
Atp5a1
Atp5b
Atp5c1
Atp5e
Atp5g2
Mtatp6
Mtatp8
Atp5h
Atp5i
Atp5f1
Atp5d
Atp5j2
Atp5j
Atp5l
Atp5o
Atpif1
log2(Fold Change)

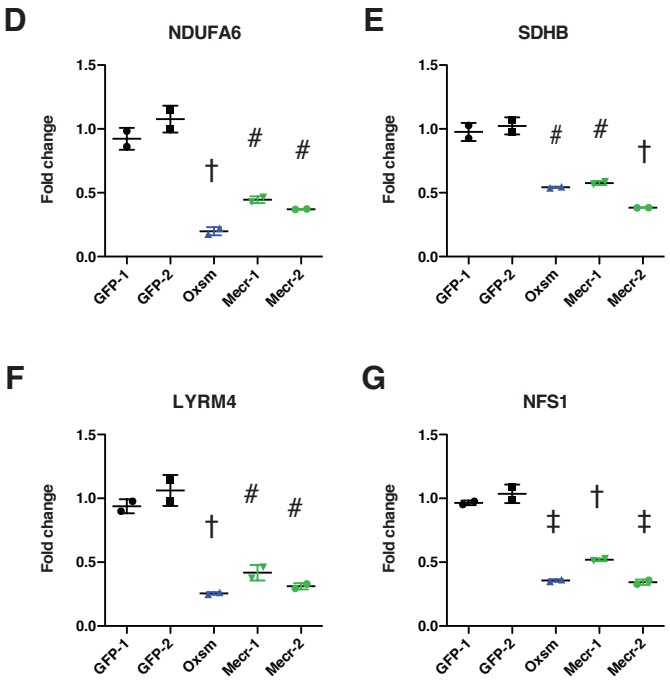
D
NDUFA6
E
SDHB
F
LYRM4
G
NFS1
Fold change
GFP-1
GFP-2
Oxsm
Mecr-1
Mecr-2

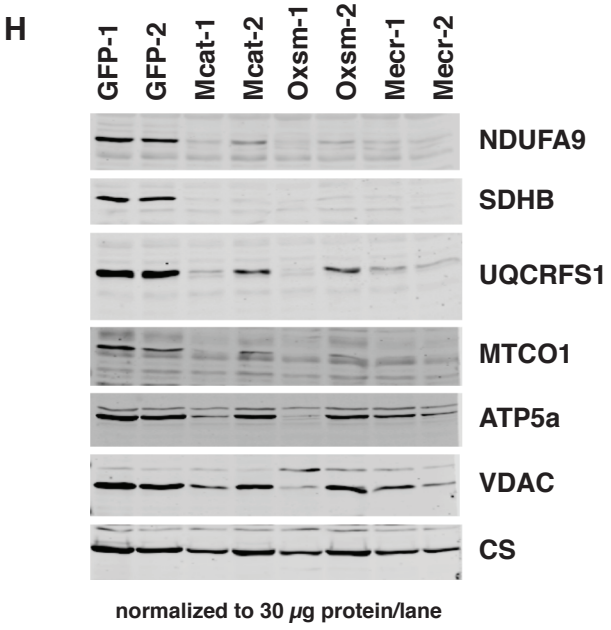
H
GFP-1
GFP-2
Mcat-1
Mcat-2
Oxsm-1
Oxsm-2
Mecr-1
Mecr-2
NDUFA9
SDHB
UQCRFS1
MTCO1
ATP5a
VDAC
CS
normalized to 30 μg protein/lane

Figure 3

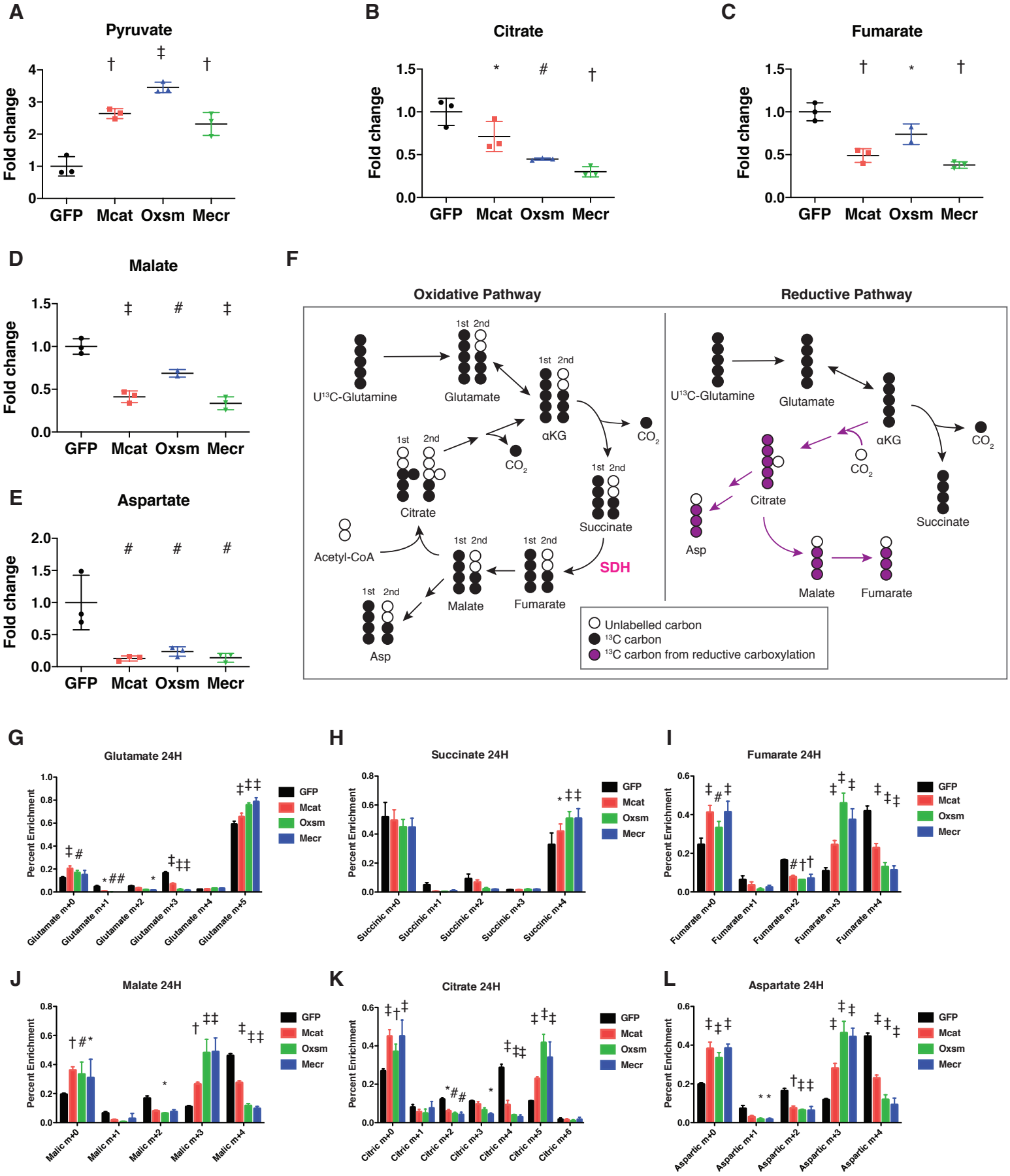
A
Pyruvate
Fold change
GFP
Mcat
Oxsm
Mecr
B
Citrate
C
Fumarate
D
Malate
E
Aspartate
F
Oxidative Pathway
Reductive Pathway
U13C-Glutamine
Glutamate
αKG
CO2
Citrate
Succinate
Acetyl-CoA
Malate
Fumarate
Asp
SDH
1st 2nd
Unlabelled carbon
13C carbon
13C carbon from reductive carboxylation
G
Glutamate 24H
Glutamate m+0
Glutamate m+1
Glutamate m+2
Glutamate m+3
Glutamate m+4
Glutamate m+5
H
Succinate 24H
Succinic m+0
Succinic m+1
Succinic m+2
Succinic m+3
Succinic m+4
I
Fumarate 24H
Fumarate m+0
Fumarate m+1
Fumarate m+2
Fumarate m+3
Fumarate m+4
J
Malate 24H
Malic m+0
Malic m+1
Malic m+2
Malic m+3
Malic m+4
K
Citrate 24H
Citric m+0
Citric m+1
Citric m+2
Citric m+3
Citric m+4
Citric m+5
Citric m+6
L
Aspartate 24H
Aspartic m+0
Aspartic m+1
Aspartic m+2
Aspartic m+3
Aspartic m+4
Percent Enrichment

Figure 4

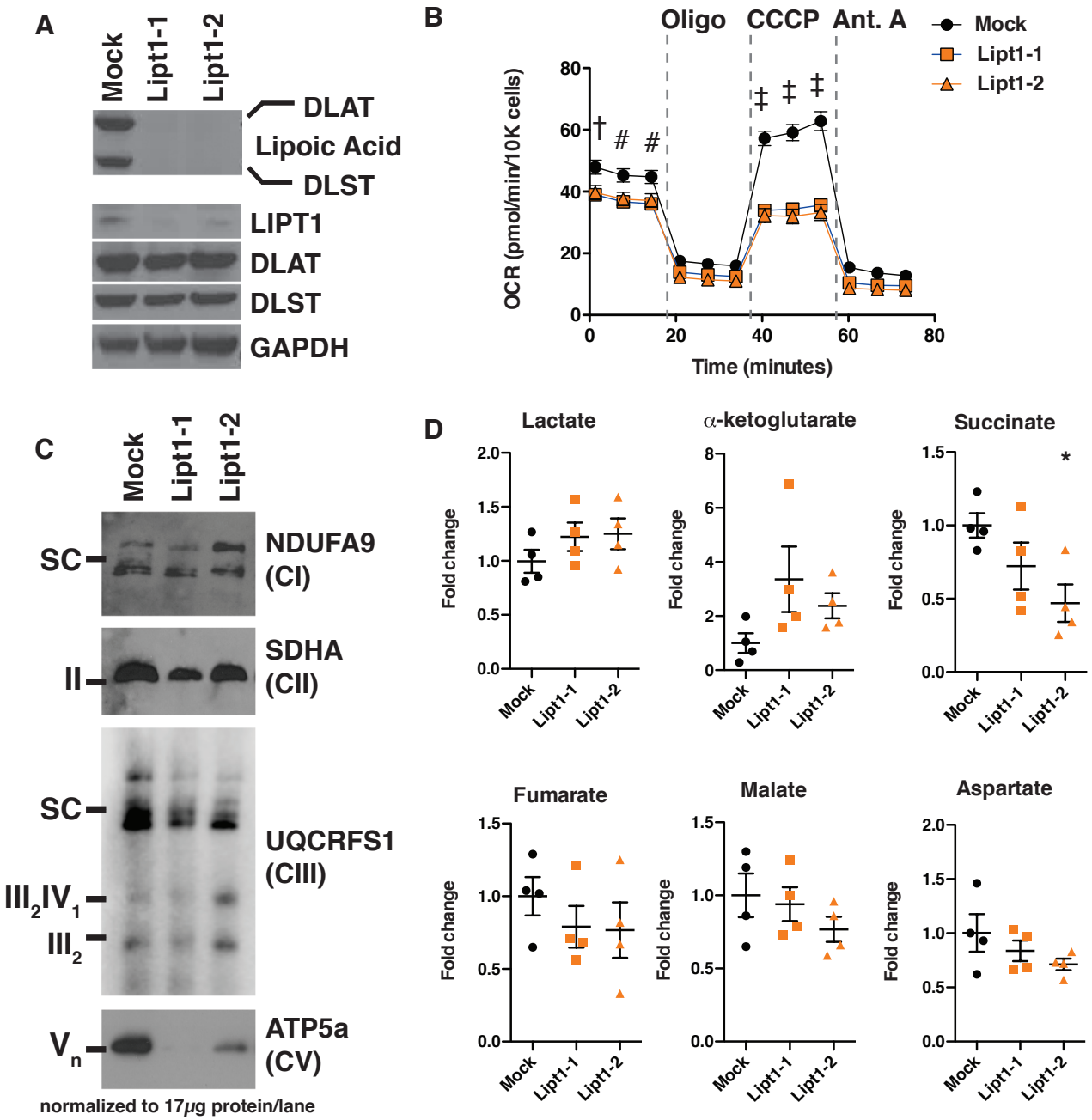
A
Mock
Lipt1-1
Lipt1-2
DLAT
Lipoic Acid
DLST
LIPT1
DLAT
DLST
GAPDH
B
Oligo
CCCP
Ant. A
Mock
Lipt1-1
Lipt1-2
OCR (pmol/min/10K cells)
Time (minutes)
C
Mock
Lipt1-1
Lipt1-2
SC
NDUFA9
(CI)
II
SDHA
(CII)
SC
III2IV1
III2
UQCRFS1
(CIII)
Vn
ATP5a
(CV)
normalized to 17μg protein/lane
D
Lactate
α-ketoglutarate
Succinate
Fumarate
Malate
Aspartate
Fold change
Mock
Lipt1-1
Lipt1-2
E
Fumarate 24H
Malate 24H
Fractional Enrichment
Fumarate m+0
Fumarate m+1
Fumarate m+2
Fumarate m+3
Fumarate m+4
Malate m+0
Malate m+1
Malate m+2
Malate m+3
Malate m+4
Mock
Lipt1-1
Lipt1-2

Figure 5

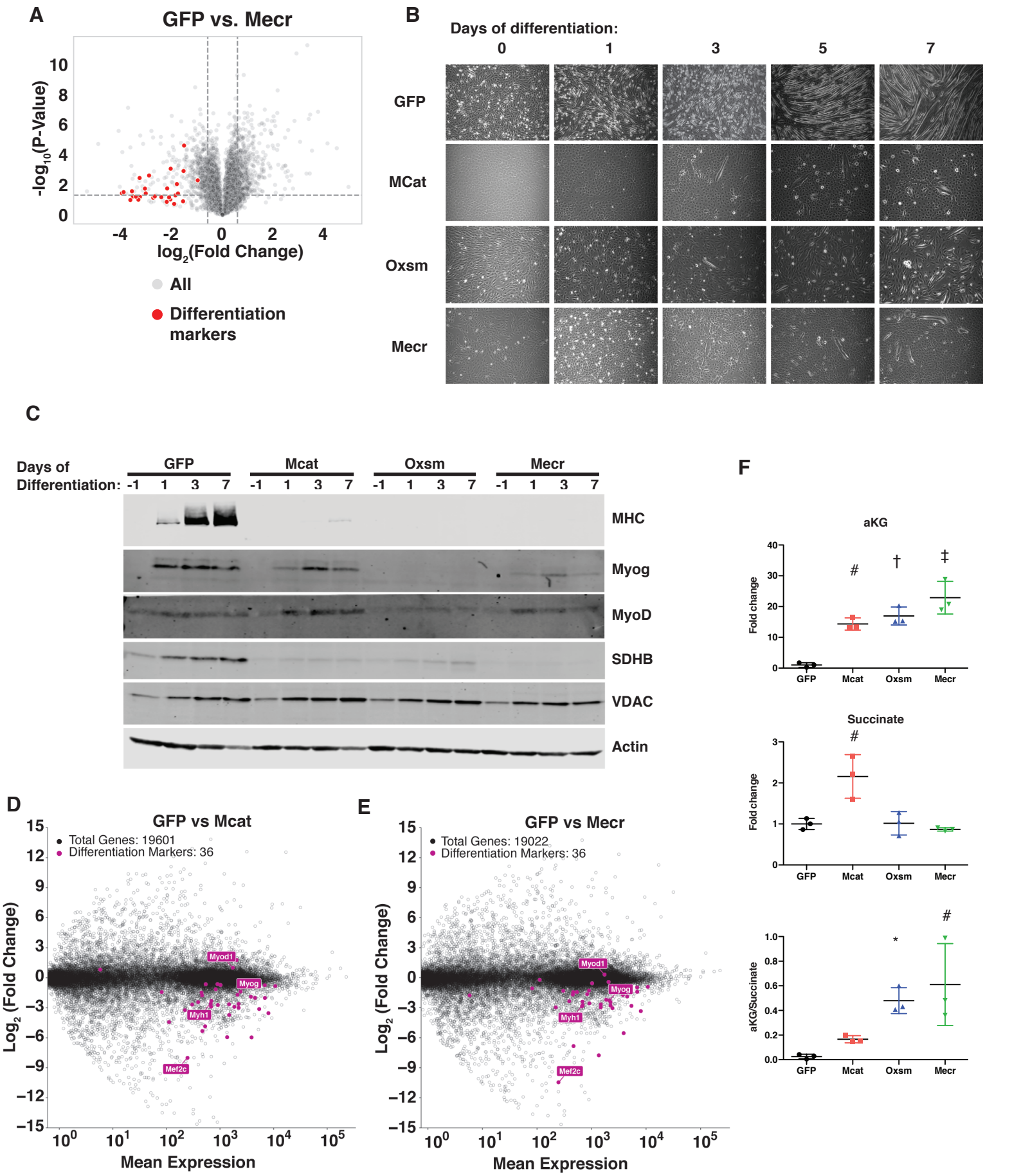
A
GFP vs. Mecr
-log10(P-Value)
log2(Fold Change)
All
Differentiation markers
B
Days of differentiation:
0
1
3
5
7
GFP
MCat
Oxsm
Mecr
C
Days of Differentiation:
GFP
Mcat
Oxsm
Mecr
-1 1 3 7
MHC
Myog
MyoD
SDHB
VDAC
Actin
D
GFP vs Mcat
Total Genes: 19601
Differentiation Markers: 36
Log2 (Fold Change)
Mean Expression
Myod1
Myog
Myh1
Mef2c
E
GFP vs Mecr
Total Genes: 19022
Differentiation Markers: 36
Log2 (Fold Change)
Mean Expression
Myod1
Myog
Myh1
Mef2c
F
aKG
Fold change
GFP
Mcat
Oxsm
Mecr
Succinate
Fold change
aKG/Succinate

Figure 6

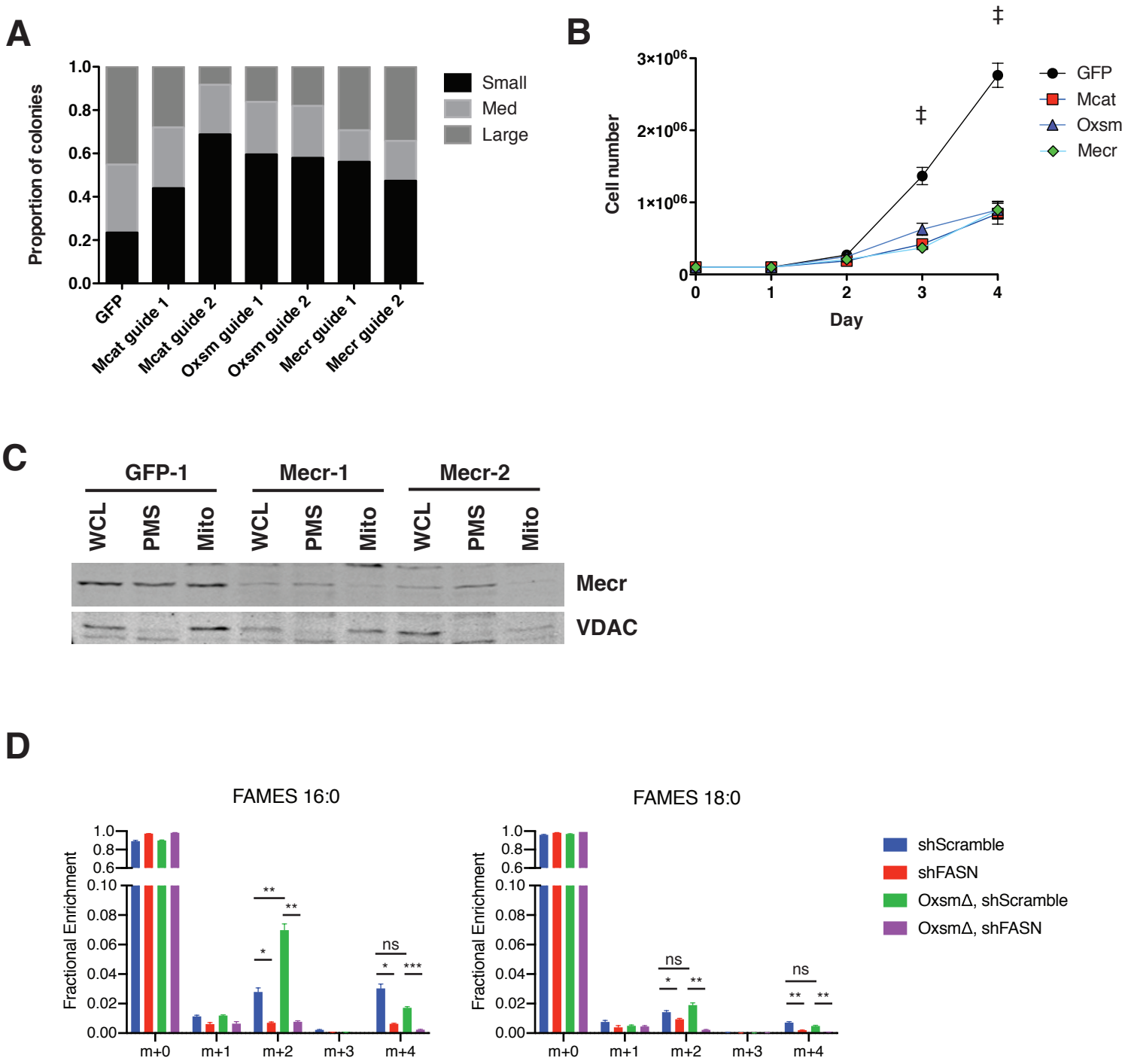

Supplementary Figure 1

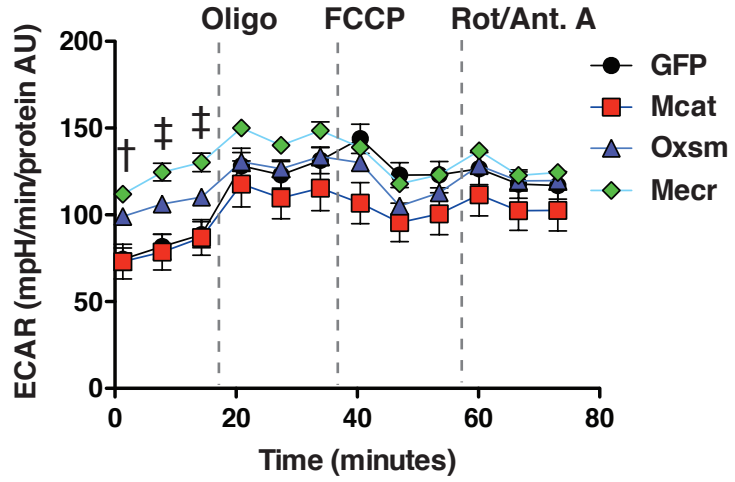

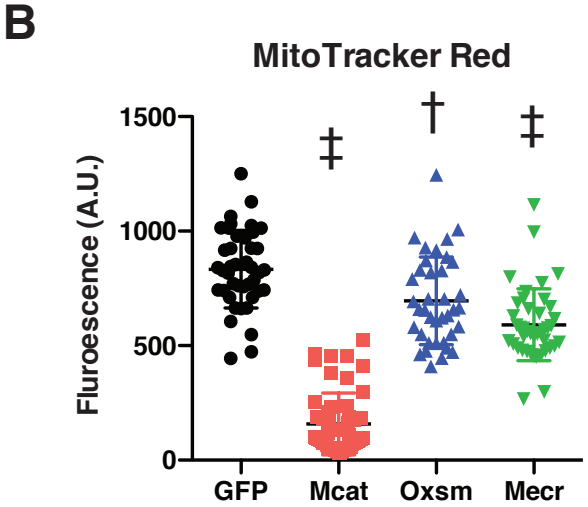

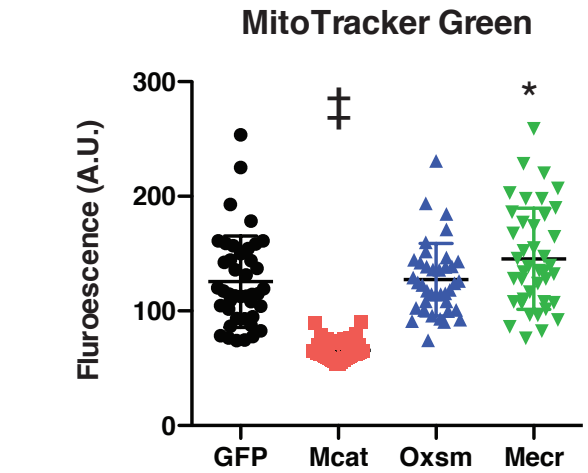

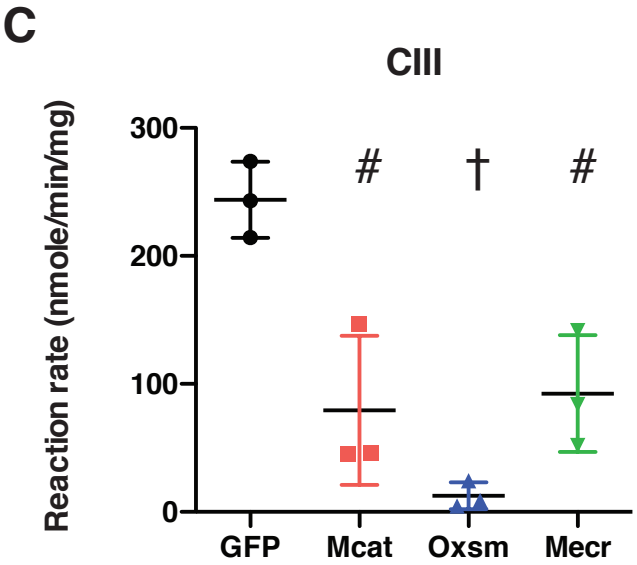

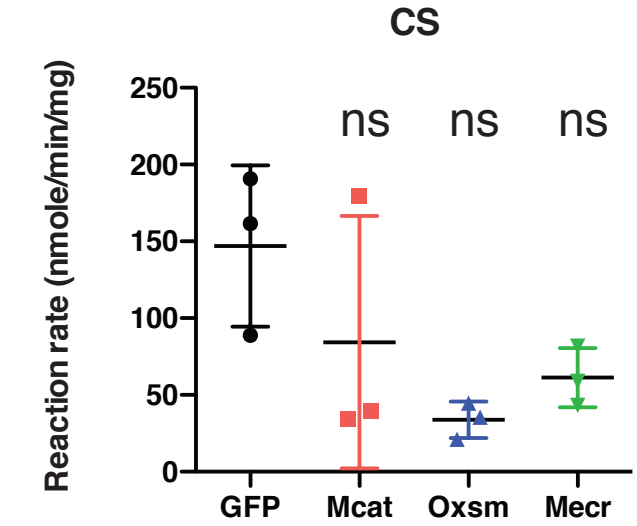

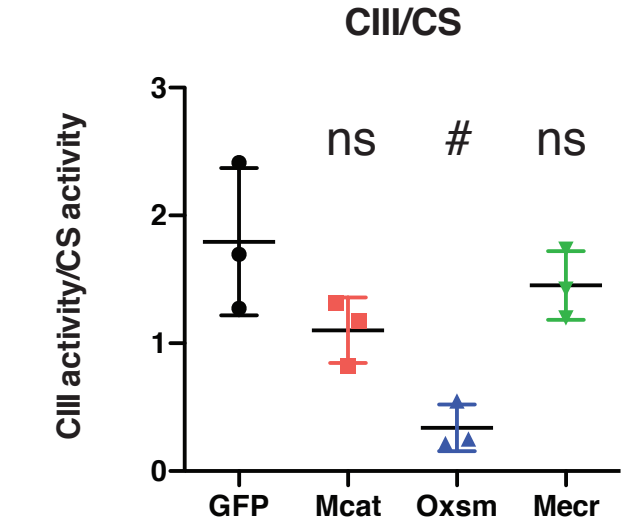

Supplementary Figure 2

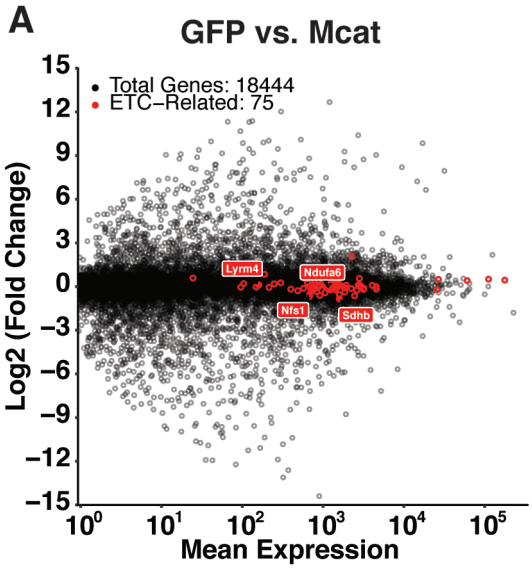

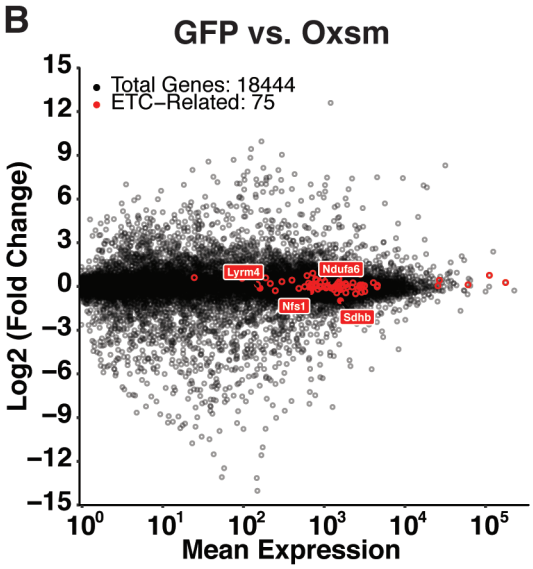

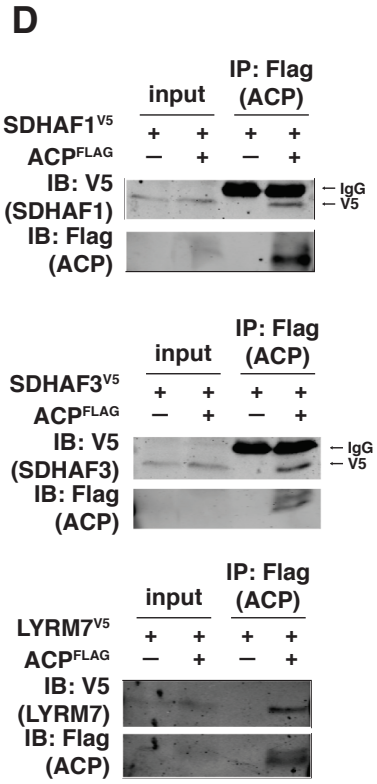

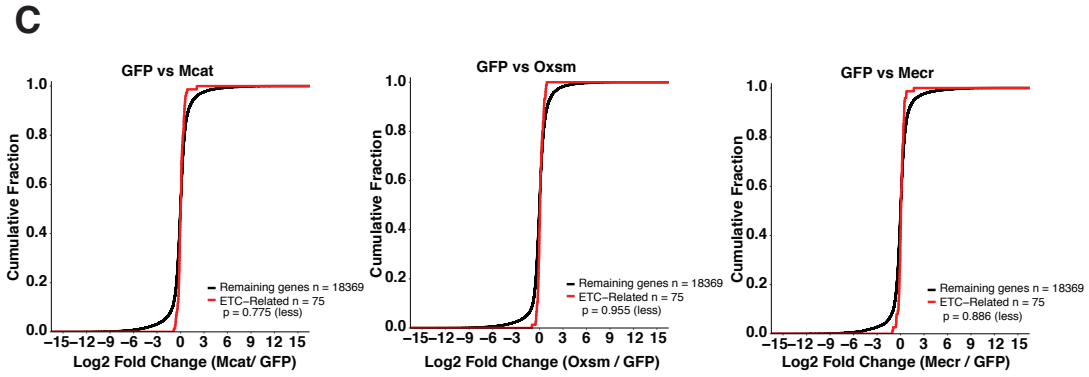

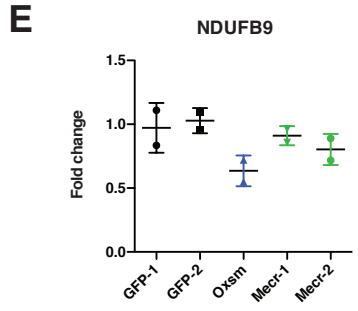

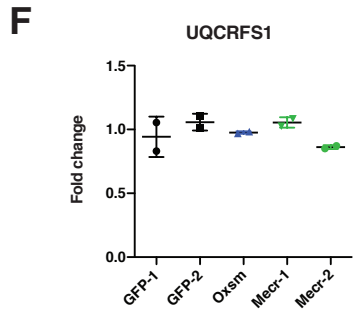

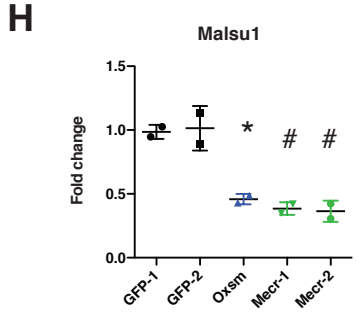

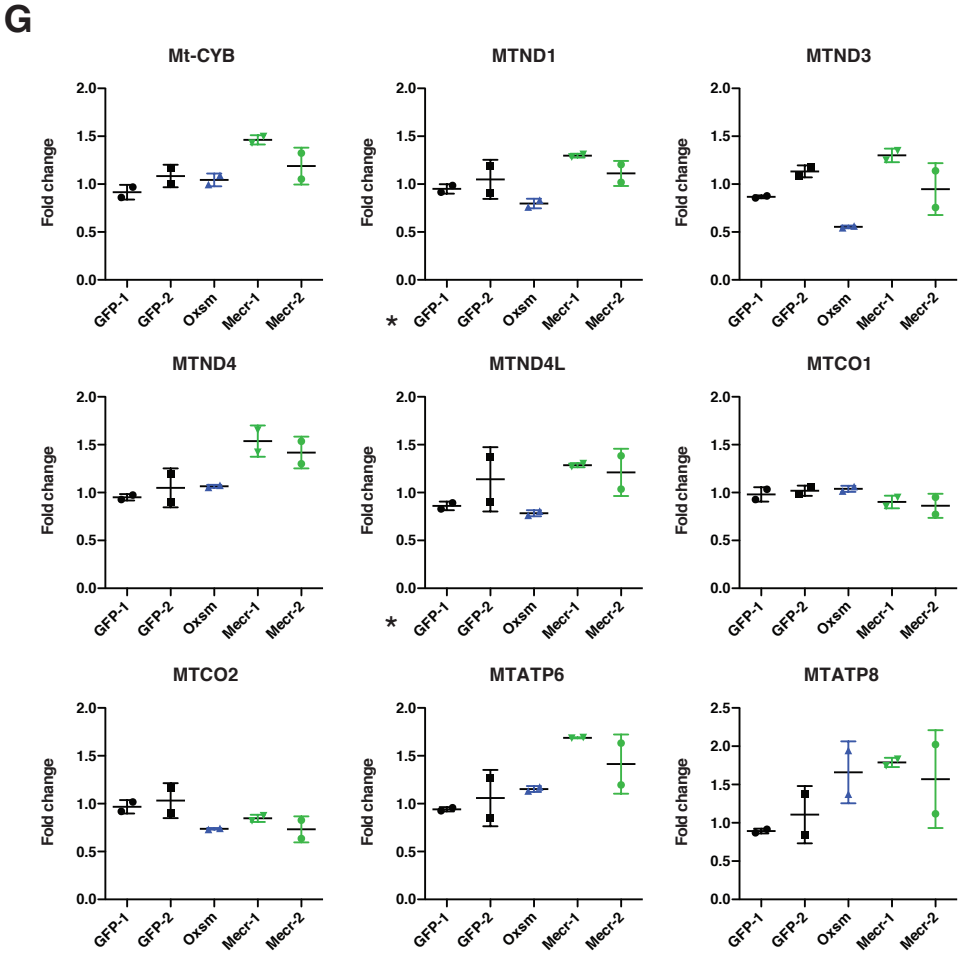

Supplementary Figure 3

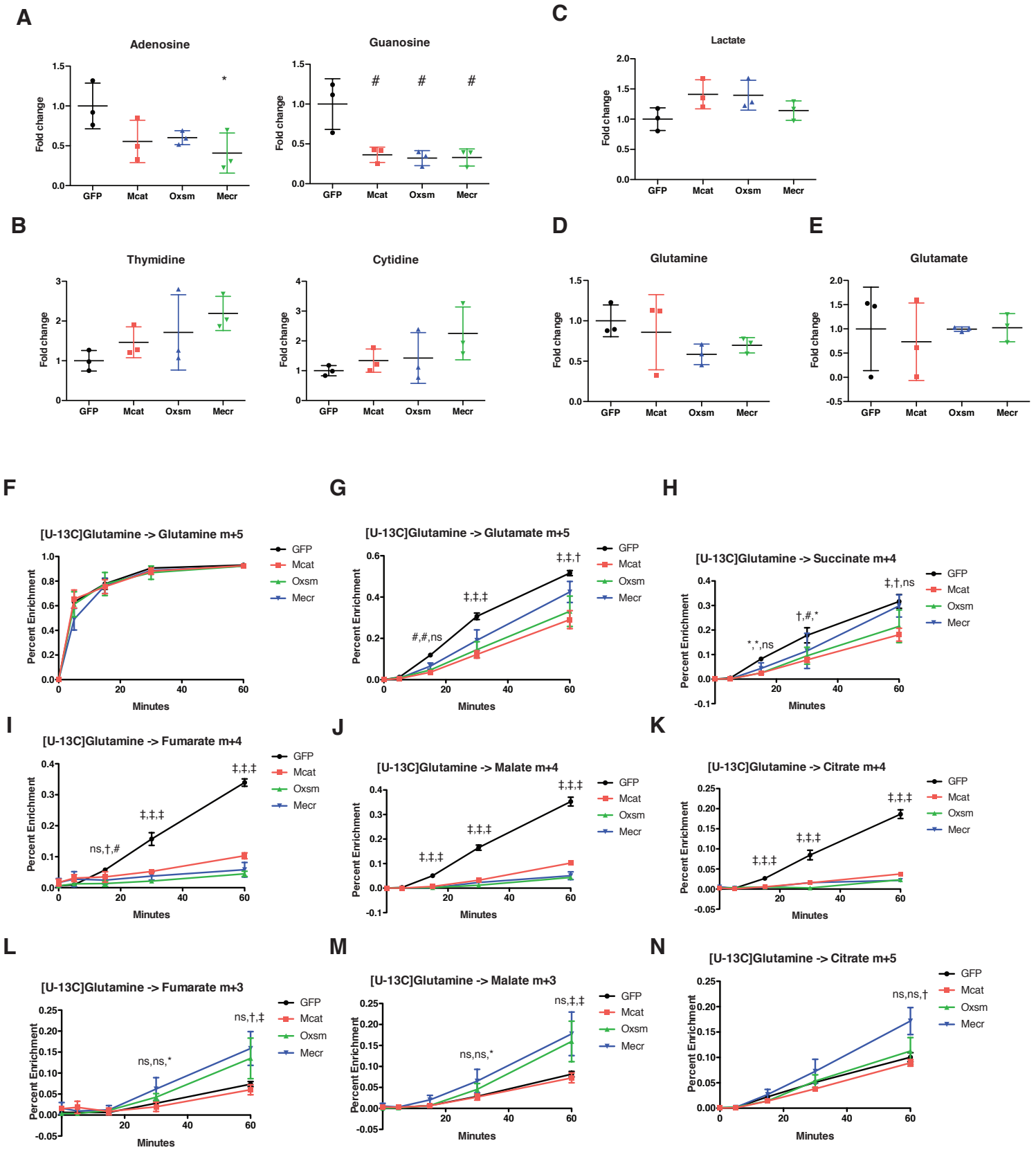

Supplementary Figure 4

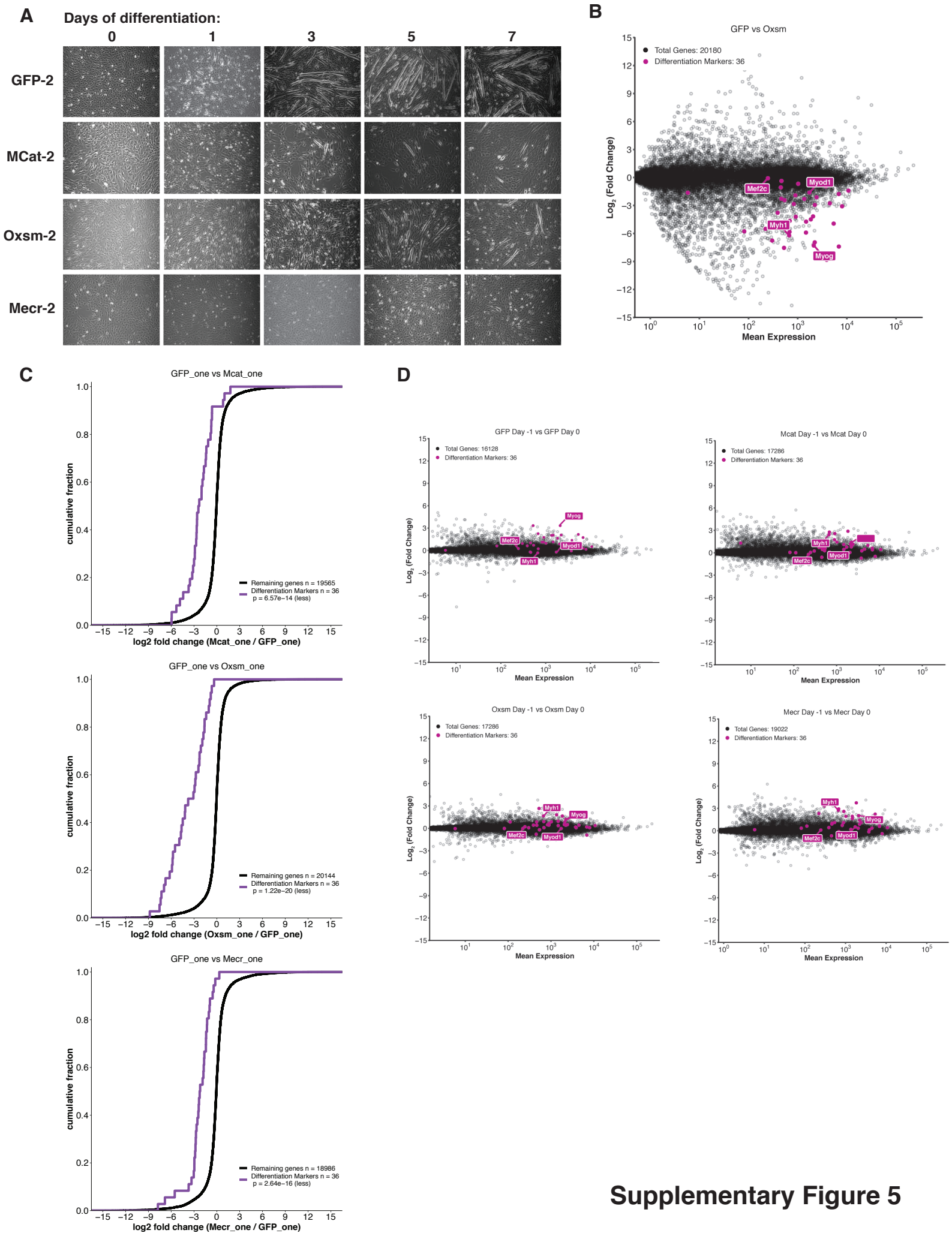

Supplementary Figure 5